Modeling and Measuring Eccentricity in Binary Black Hole Inspirals

LIGO Student Undergraduate Research Fellowship, California Institute of Technology

Simona Miller

Smith College, Northampton, MA 01063

Mentors: Jonah B. Kanner, Alan J. Weinstein, and Thomas Callister

LIGO Laboratory, Caltech, Pasadena, CA 91125

(Dated: September 25, 2018)

Abstract

Due to the emission of gravitational wave (GW) radiation, most compact binaries are expected to circularize before emitting GWs in the LIGO frequency band. However, if a binary black hole system resulted from dynamical capture or hierarchal triple interactions close to the end of its life, there is a probability that the system could retain non-negligible eccentricity while in the LIGO band. As such, observing eccentricity from a gravitational wave signal could be a clear signature of dynamical origins. Despite the observational importance of eccentricity, the techniques needed to detect and characterize it currently remain in their early stages. We model eccentric binary black holes in the time domain and assess the detectability and identifiability of eccentric binary black hole systems, aiming to discover how accurately we can estimate parameters of an eccentric waveform. We employ a variety of data analysis techniques, including calculating overlaps between waveforms, constructing likelihood distributions, and using Bayesian parameter estimation.

I. INTRODUCTION

To date, LIGO's gravitational wave detectors have observed gravitational waves from six binary black holes and one binary neutron star [1–6]. The observed binary black hole (BBH) coalescences follow a consistent pattern: the systems have quasi-circular orbits that decrease in radius and increase in frequency as they lose energy in the form of gravitational radiation. All observed gravitational waves from BBH fit a "chirp" waveform while within the LIGO frequency band (a minimal orbital frequency of 10 Hz, or a gravitational wave frequency of 20 Hz); their amplitude and frequency increase as the binary evolves [7]. The plots in Figure 1 show predicted chirp waveforms; Figure 2 shows an "actual" waveform, specifically the bandpassed, filtered data from GW150914, LIGO's first detected gravitational wave [8]. Although Einstein's theory of General Relativity predicts that eccentric systems will produce qualitatively different waveforms, LIGO data analysis methodology presently uses waveform templates that assume a negligible eccentricity; highly eccentric BBH could go undetected with current technology. Additionally, many properties of BBH are currently calculated with the assumption of circular orbits, such as their masses and distance from Earth [7]. Identifying eccentricity could make such calculations more accurate, and will yield a better understanding BBH formation mechanisms and the stellar environments in which they reside.

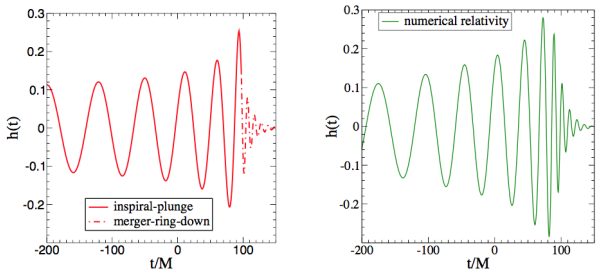

FIG. 1: Chirp waveform predicted using effective-one-body approach (left) and numerical relativity simulations (right) for same initial conditions. Figure from [7]

In this report, I describe the exploration of the "eccentricity problem" that I have engaged in this summer. Section II outlines the objectives for this project. In Section III, I describe binary black hole formation mechanisms that could result in measurable eccentricity. In Section IV, I discuss how orbital period, semi-major major axis, and eccentricity evolve over time during an eccentric inspiral. Section V introduces waveforms for BBH with eccentricity;

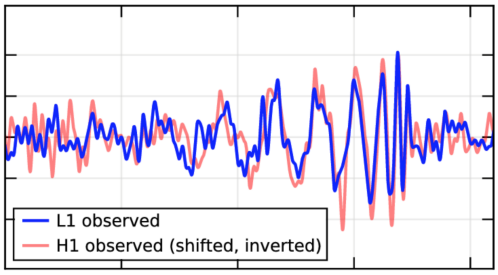

FIG. 2: Strain (h(t)) plotted against time (t) for GW150914, LIGO's first GW detection. This plot shows data that has been filtered, i.e. subject to band-passing and line removal. L1 is the data from the Livingston, Louisiana detector; H1 is the data from the Hanford, Washington detector. Figure from [8]

here I present the equations for the emitted gravitational wave strain and describe unique characteristics of such waveforms. In Section VI, I discuss the characteristic evolution of the phase-angle of eccentric waveforms. Section VII is an introduction to the Bayesian framework used for data analysis. Sections VIII - X discuss the primary results from the project: the results from recovering eccentric signals using a variety of waveform families (circular non-spinning, eccentric non-spinning, and circular precessing-spin). Section XI lists conclusions and future work.

II. OBJECTIVES

The aim of this project is to build on existing research to assess detectability and identifiability of eccentric binary black holes. We focus on three groups of questions:

1. What are key features of eccentric waveforms in the time and frequency domains? In Python, we create a waveform family for a range of initial eccentricities using a lowest order Post-Newtonian approximation and compare these waveforms to existing models in LALSuite [9]. In the phase-angle domain, how do these eccentric waveforms deviate from quasi-circular waveforms?

2. Does eccentricity make GW signals from BBH harder to detect? Specifically, how much signal-to-noise ratio (SNR) can be lost if a search pipeline uses a quasi-circular binary template (with no higher order effects) to capture an eccentric binary merger event? We calculate the lost SNR at a variety of the initial eccentricities (e.g., eccentricity at GW frequency of 20 Hz) and masses of the two black holes

3. How well can the eccentricity parameter be extracted from an observed event, using likelihood distributions, Bayesian parameter estimation and MCMC techniques? As a function of SNR and eccentricity, with what confidence can we say eccentricity is nonzero? Are there any degeneracies between eccentricity and other internal parameters (e.g. mass) that affect our ability to extract the eccentricity parameter from a data set? Furthermore, are there any degeneracies between eccentricity and other higher order effects like spin precession?

III. BINARY BLACK HOLE FORMATION MECHANISMS

Binary black holes have several formation mechanisms, the two most widely understood being common binary evolution and dynamical interaction in dense stellar environments such as globular clusters or galactic nuclei. Evolutionary trajectories for both formation mechanisms predict that under most circumstances, the orbits of BBH systems will have circularized by the time their emitted gravitational radiation is within the LIGO band. However, if a BBH forms via dynamical capture with large eccentricity and/or extremely close to the end of its lifetime (i.e., a small periastron), there *is* a probability that the system retains non-negligible eccentricity while still emitting GWs in the LIGO band [1]. Dense stellar regions, such as galactic nuclei and globular clusters that have undergone mass segregation, are prime spots for dynamical BH-BH capture. In such settings, individual black holes can become gravitationally bound during close passage as energy is lost in the form of a GW burst [10].

Another possibility for observing an eccentric BBH in the LIGO band is via a hierarchal triple, a quasi-stable three-body system where one BBH is orbited by another black hole. Eccentricity can be produced in hierarchal triples through angular momentum exchange from the inner binary and the larger system, in what is known as the Kozai-Lidov mechanism [11, 12].

IV. ECCENTRIC BINARY INSPIRAL EVOLUTION

The evolution of compact binary coalescences (CBC) can be broken into three phases: inspiral, merger, and ringdown. We focus on the inspiral phase, as once the CBC enters

merger eccentricity no longer produces distinguishable effects. The inspiral phase is the longest phase in a CBC, ending when the objects reach their innermost stable circular orbit (ISCO). For black holes without spin, this occurs at the following condition for semi-major axis length a:

$$a_{ISCO} = 6\ \frac{G\,(\,m_1\,+\,m_2\,)}{c^2} \quad . \tag{1}$$

As the binary emits gravitational waves, its orbital period P_{orb} and eccentricity e evolve during the inspiral phase as described by the following coupled equations [13]:

$$\dot{P}_{orb} = -\frac{192\pi}{5c^5}\left(\frac{2\pi G}{P_{orb}}\right)^{5/3}\frac{m_1 m_2}{(m_1+m_2)^{1/3}}\left(1+\frac{73}{24}e^2+\frac{37}{96}e^4\right)\left(1-e^2\right)^{-7/2} \quad , \tag{2}$$

$$\dot{e} = -\frac{608\pi}{15c^5}\frac{e}{P_{orb}}\frac{m_1 m_2}{(m_1+m_2)^{1/3}}\left(1+\frac{121}{304}e^2\right)\left(1-e^2\right)^{-5/2} \quad . \tag{3}$$

It is important to note that these equations ignore spin effects and higher order effects, such as spin precession or higher order modes. By integrating these equations, orbital period and eccentricity can be related by [13]:

$$c_0 P^{19/9} = \frac{e^2}{(1-e^2)^{19/6}}\left(1+\frac{121}{304}e^2\right)^{145/121} \tag{4}$$

where c_0 is a constant determined by the initial conditions of the orbit. Numerically solving (2) and (3) with the initial conditions of $P_{orb,0} = 0.3s$ and $e_0 = 0.4$ yields the time series for orbital period and eccentricity shown in Figure 3. Additionally, a time series for semi-major axis length a was calculated from Kepler's Third Law (also seen in Figure 3),

$$a = \left[{P_{orb}}^2\left(\frac{G(m_1+m_2)}{4\pi^2}\right)\right]^{1/3} \quad . \tag{5}$$

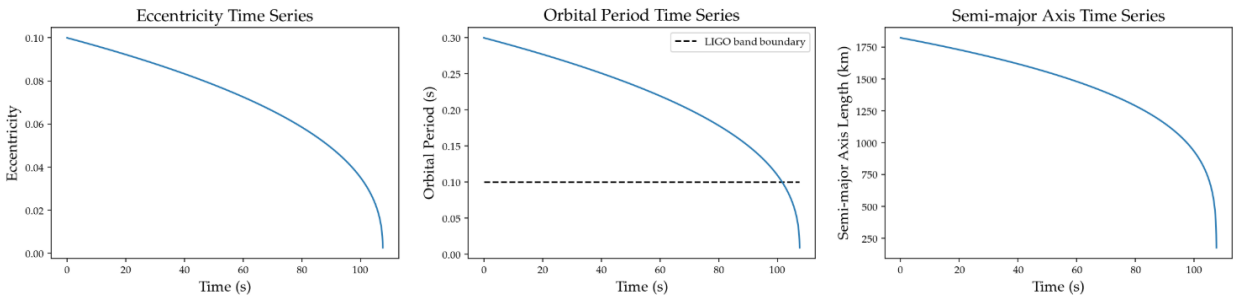

FIG. 3: Time evolution of eccentricity, orbital period, and semi-major axis for BBH system with initial orbital period of 0.3 seconds and initial eccentricity of 0.1. ($m_1 = m_2 = 10M_\odot$)

The shape of the time series' for orbital period and eccentricity depend on initial orbital period, initial eccentricity, chirp mass, and mass ratio. As initial eccentricity increases, the duration of the CBC in the LIGO band decreases; the BBH reaches ISCO in a shorter amount of time. As total mass increases and/or mass ratio decreases, the duration of the BBH in the LIGO band also decreases. These patterns can be seen in Figures 4, 5, and 6.

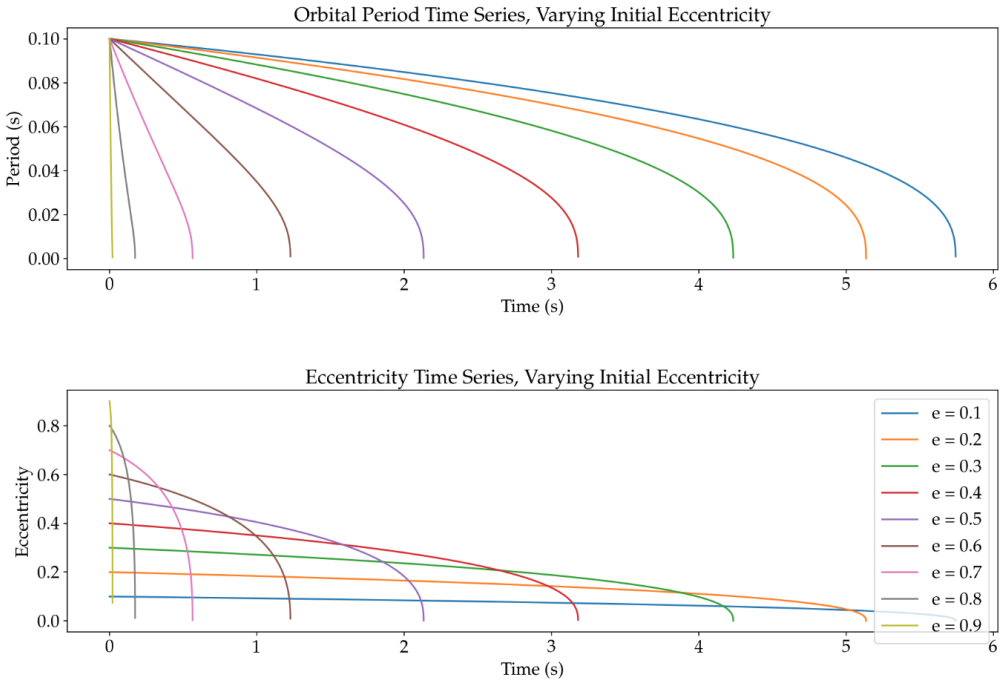

FIG. 4: Orbital period time series and eccentricity time series with varying values of eccentricity at an initial period of 0.1s. ($m_1 = m_2 = 10M_\odot$)

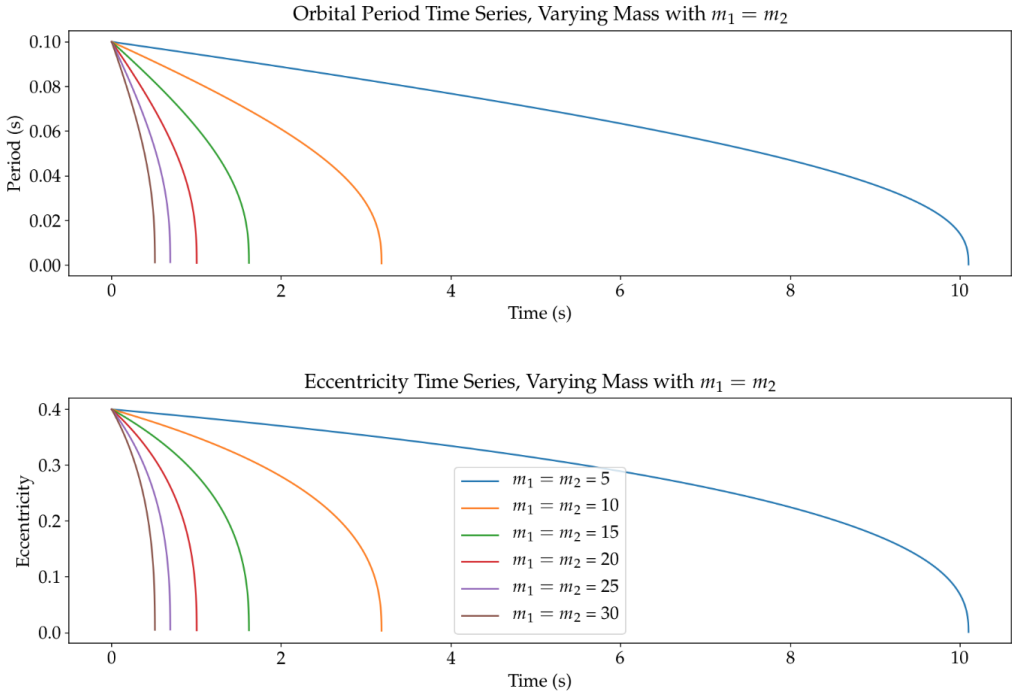

FIG. 5: Orbital period time series and eccentricity time series with varying total masses. All series have a mass ratio of 1.

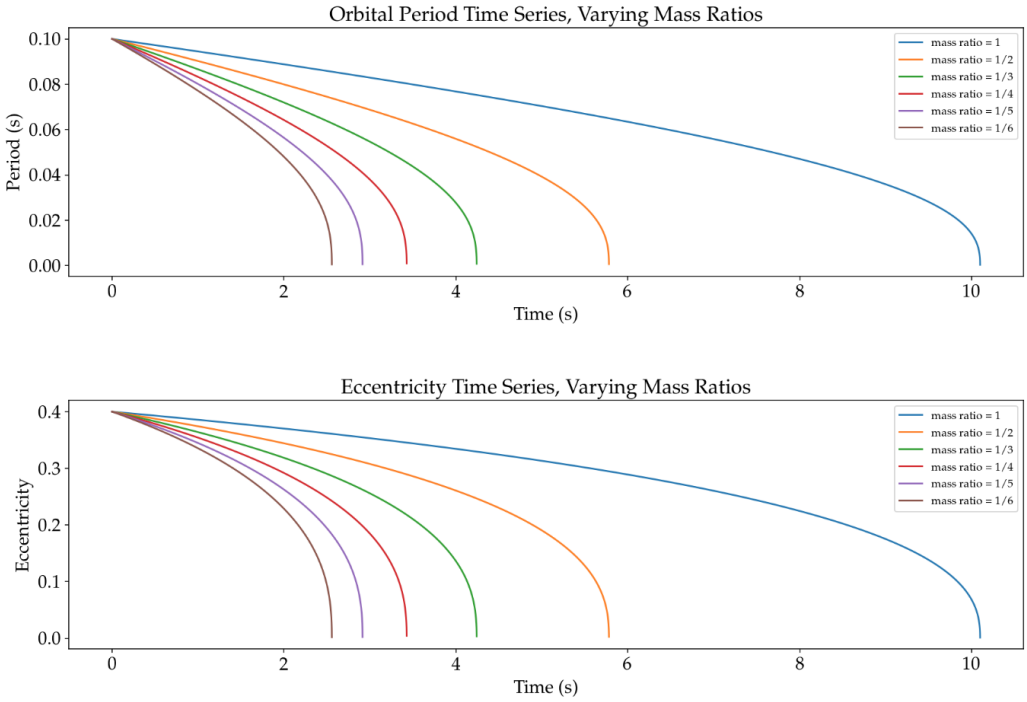

FIG. 6: Orbital period time series and eccentricity time series with varying mass ratios. m_1 always equals 5 solar masses, and m_2 ranges from 5 solar masses to 35 solar masses in increments of 5 solar masses.

V. WAVEFORM MODELS

Once a dynamically captured BH pair is in eccentric orbit, a GW burst will be emitted every time the pair passes at a close encounter (i.e. at periastron). This causes the semi-major axis (a) and eccentricity (e) to decrease with time, while orbital frequency increases with time. After sufficient energy is lost through gravitational radiation, the BH pair will merge.

A. Generating a Waveform Model using Python

Gravitational wave strain, $h(t)$ is generated by an accelerating quadrupole moment, I: $h(t) \sim \frac{d^2}{dt^2}(I)$ where $I = \int \rho\, r^2\, dV$. Without taking the effects of eccentricity into account, this strain from a BBH is given in equation (6) where d is the distance to the source, a is the distance between the orbiting bodies, m_1 and m_2 are the masses of the BH, and $\varphi(t)$ is the phase evolution:

$$h(t) = \frac{4\ (m_1 + m_2)^2}{a\ d} cos(2\,\varphi(t)) \quad . \tag{6}$$

Note that this equation is given in units where G = c = 1. In traditional SI units, there is a factor of G^2 in the numerator and c^4 in the denominator.

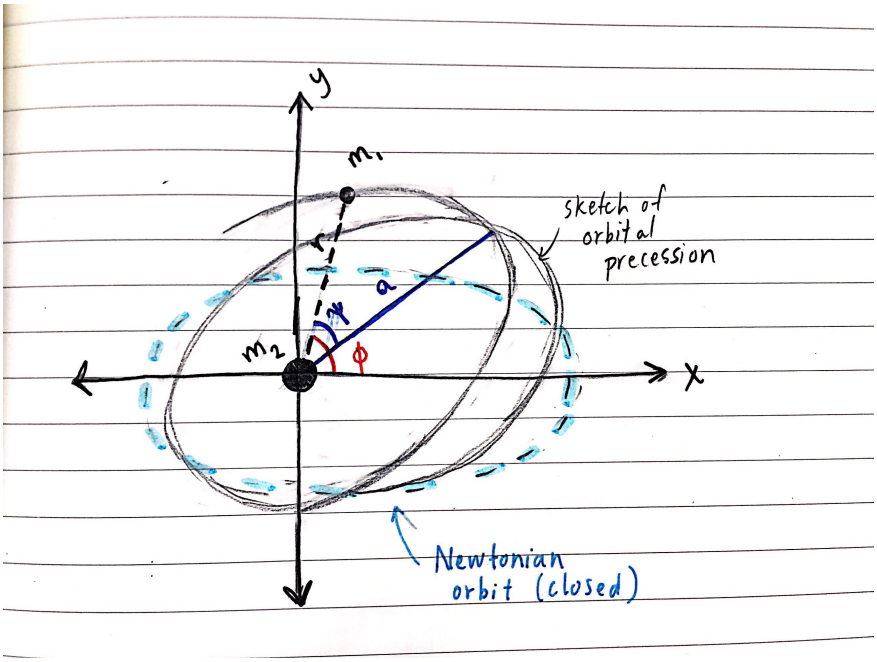

FIG. 7: Diagram showing difference between ϕ and ψ in an eccentric binary. ϕ is the angle between r and a fixed x-axis in m_2's (the larger mass) frame of reference, while ψ is the angle between r and the precessing semi-major axis a.

However, BBH in eccentric orbits produce a more complicated GW strain, due to emitting GW bursts at periastron passage, periastron precession, and the consequent oscillating distance between the orbiting bodies. The location of a body in an eccentric orbit can be defined using two angles: ψ and ϕ. ψ, also known as the true anomaly, corresponds to the radial period; it is taken with respect to the semi-major axis. However, due to periastron precession, the semi-major axis is itself rotating. ϕ takes this into account; it corresponds to the orbital period. It is taken from a fixed axis in space, while the axis from which ψ is taken is rotating. See Figure 7 for a visualization. Taking these effects into account, the plus and cross polarizations for gravitational wave strain from an eccentric BBH system are, in units where G = c = 1:

$$h_+(t) = \frac{\mu}{2\,d}\Bigg(\Big[1\;-\;2\,cos\big(2\theta\big)\,cos^{\,2}\big(\phi(t)\big) - 3\,cos\big(2\,\phi(t)\big)\Big]\dot{r}^{\,2}(t) + \Big(3\;+\;cos\big(2\theta\big)\Big)\Big[2\,cos\big(2\,\phi(t)\big)\,\dot{\phi}^{\,2}(t) + \;sin\big(2\,\phi(t)\big)\,\ddot{\phi}(t)\Big]r^{\,2}(t) + \Big[4\Big(3\;+\;cos\big(2\theta\big)\Big)\,sin\big(2\,\phi(t)\big)\dot{\phi}(t)\dot{r}(t) + \Big(1\;-\;2\,cos\big(2\theta\big)\,cos^{\,2}\big(\phi(t)\big)\;-\;3\,cos\big(2\phi(t)\big)\Big)\ddot{r}(t)\Big]r(t)\Bigg) \quad , \quad (7)$$

$$h_\times(t) = -\frac{2\,\mu\,cos(\theta)}{d}\Bigg(sin\big(2\phi(t)\big)\,\dot{r}^2(t) + \Big[cos\big(2\phi(t)\big)\,\ddot{\phi}(t)\;-\;2\,sin\big(2\phi(t)\big)\,\dot{\phi}^2(t)\Big]r^2(t) + \Big[4\,cos\big(2\phi(t)\big)\,\dot{\phi}(t)\,\dot{r}(t)\;+\;sin\big(2\phi(t)\big)\,\ddot{r}(t)\Big]r(t)\Bigg) \quad (8)$$

where μ is the reduced mass of the binary, d is the distance to the source, θ is the angle of inclination of the source, r is the distance between the two BHs, and ϕ is angle corresponding to the orbital period [14].

To solve for the strain, we need to time evolve r and ϕ, which is done using the energy and angular momentum of the system. In this derivation we use the Newtonian approximations of these quantities. The Newtonian definition of orbital energy E_{orb} for an elliptical orbit with total mass M_{tot}, reduced mass μ, and semi-major axis length a is:

$$E_{orb} = K + U = \frac{U}{2} = -\frac{G\,M_{tot}\,\mu}{2a} \quad (9)$$

where $K + U = \frac{U}{2}$ is the Virial Theorem for gravity. The Newtonian definition of orbital angular momentum L_{orb} is as follows:

$$L_{orb} = \sqrt{G\,M_{tot}\,\mu\,a\,(1\;-\;e^2)} \quad . \quad (10)$$

From these definitions, we can express the quantities of specific total energy and specific angular momentum, in geometric units (G=c=1), to be used throughout the remainder of the report:

$$E = 1 + \frac{E_{orb}}{\mu} \quad , \quad L = \frac{L_{orb}}{\mu} \quad . \tag{11}$$

The distance r between the two BH's is:

$$r = \frac{a\left(1 - e^2\right)}{1 + e\, cos\psi} \tag{12}$$

where ψ is the true anomaly of the eccentric system (see Figure 7). To generate a time series for r, we must time evolve ψ using the following equation, adapted from [14]:

$$\dot{\psi} = \frac{(1\ -\ E^2)^{1/2}}{V_t\,(1\ -\ e^2)} \Big[a\,(1 - e^2)\ - C_0\,(1 - e)\ -\ e\,a\,(1 - e^2) - e\,C_0\,(1 - e)\,cos(\psi)\Big]^{1/2} \Big[a\,(1 - e^2)\,(1 + e)\Big]^{1/2} \tag{13}$$

where the constant C_0 is given by:

$$C_0 = \frac{2}{1 - E^2} - 2a \tag{14}$$

and potential V_t is given by:

$$V_t = \frac{E\, r^4}{r^2\ -\ 2r} \tag{15}$$

.

Finally, to solve the gravitational wave strain equations given in (7) and (8), we must generate a time series for ϕ, the angle describing where a body is in its orbital period (see Figure 7). This is achieved with the following relationship between $\dot{\phi}$, specific angular momentum, and potential V_t [14]:

$$\dot{\phi} = \frac{L}{V_t} \quad . \tag{16}$$

Choosing an initial period and eccentricity, solving for the time evolution of r and ϕ, and substituting into (7) and (8) yields the time series shown in Figure 8. This model shows the unique modulation of amplitude and frequency appearing in a waveform generated by a BBH system in an eccentric orbit. This is caused by bursts of gravitational wave radiation

produced at periastron passage. As initial eccentricity increases, these bursts increase in magnitude. Additionally, just like non-eccentric waveforms, this model shows the characteristic chirp behavior of a CBC: amplitude and frequency of the GW strain increase as the binary evolves.

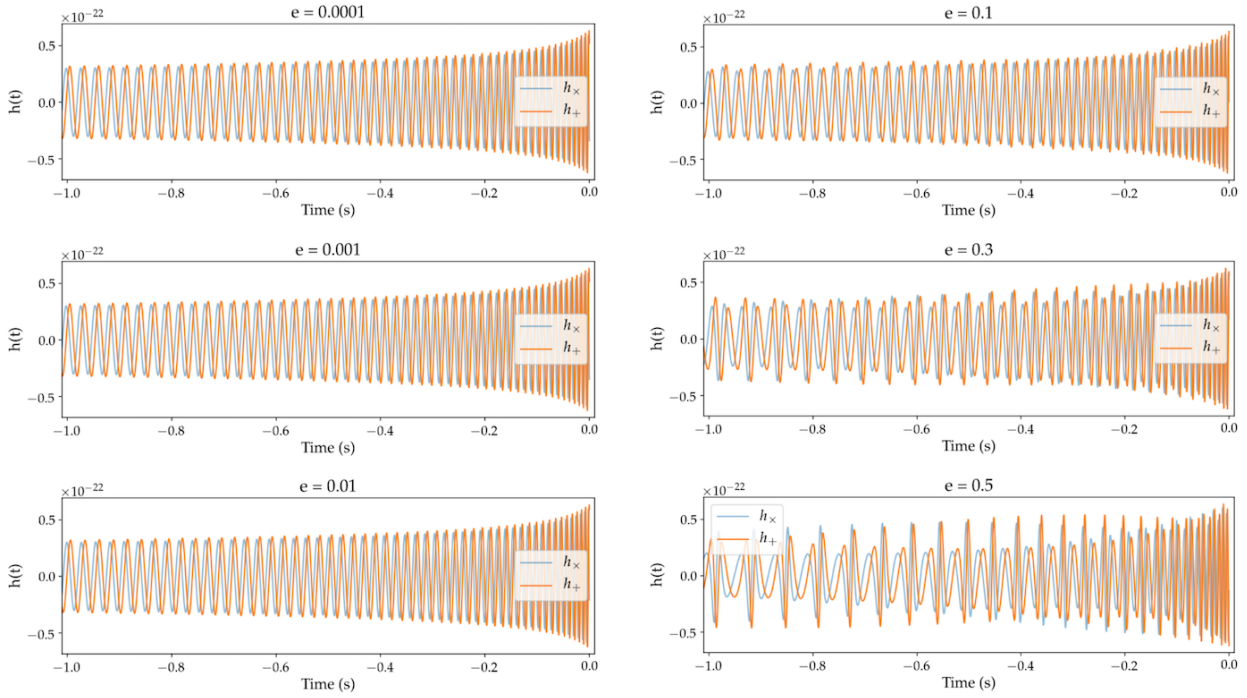

FIG. 8: Time series waveforms generated by the model described in Section V A. with initial orbital period $P_0 = 0.1s$ and initial eccentricities e_0=[0.0001, 0.001, 0.01, 0.1, 0.3, 0.5]. All waveforms are from a source with a distance of 1000 megaparsecs, masses $m_1 = m_2 = 10M_\odot$, and an inclination angle $\theta = \pi/4$. All plots show the final second before merger.

Although the model I created captures the key qualitative features of an eccentric BBH inspiral, the Newtonian approximations made for energy and angular momentum prevent it from being quantitatively accurate. Future work for this project might include improving this waveform model. Because of this inaccuracy, the EccentricTD and EccentricFD models (see Section V B.) are used for data analysis in the remainder of this report. See Section V C for quantitative measurements of this discrepancy.

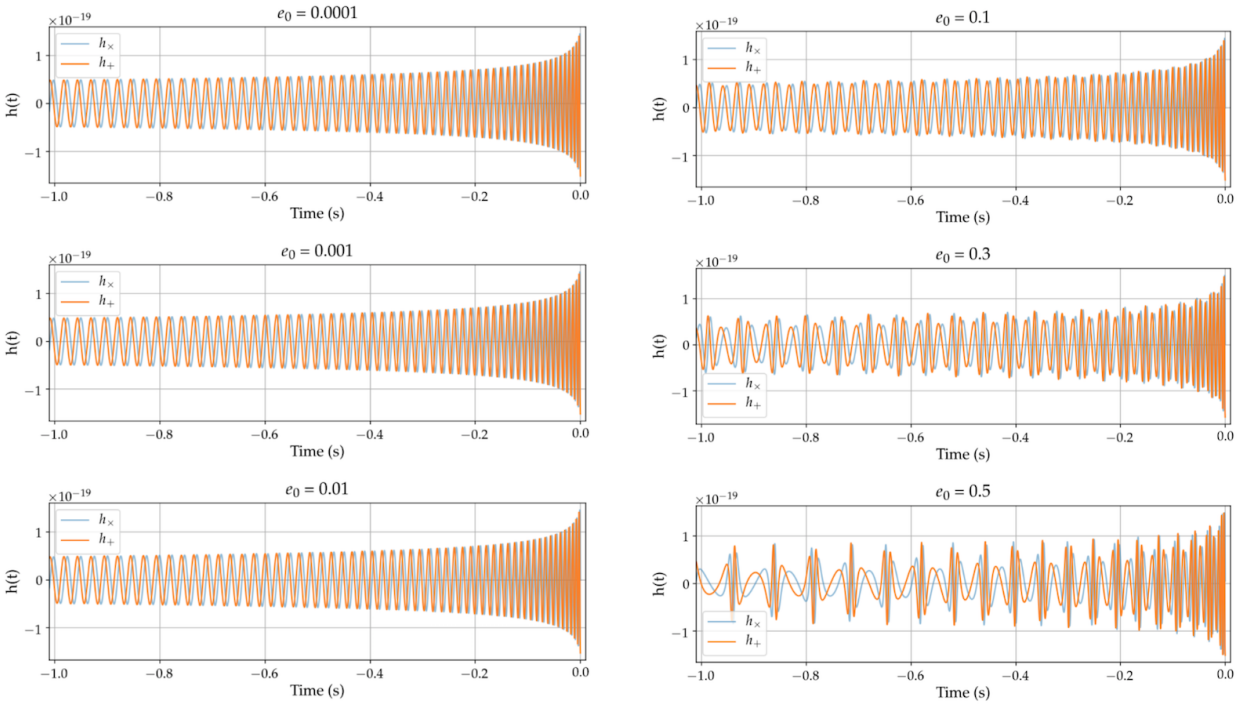

FIG. 9: Time series waveforms generated with the EccentricTD approximant at initial eccentricities e_0=[0.0001, 0.001, 0.01, 0.1, 0.3, 0.5]. All waveforms are from a source with a distance of 1 megaparsec and masses $m_1 = m_2 = 10M_\odot$. All plots show the final second before merger. Approximant from [9].

B. Existing Models

Presently, only one waveform model in the time domain - EccentricTD - and one model in the frequency domain - EccentricFD - that include the effects of eccentricity exist in the LIGO Scientific Collaboration Algorithm Library Suite (LALSuite) [9]. Like the waveforms generated in Section V A, these waveform families only model the inspiral phase of a CBC, meaning they exclude merger and ringdown, and ignore component spin. Examples of time series plotted with EccentricTD and frequency series plotted with EccentricFD with varying initial eccentricity values can be seen in Figures 9 and 10. Note that the right three plots in Figure 10 are noisy. At this time we are unsure if this effect is due to physical reasons, inherent problems with the EccentricFD waveform, under-sampling in the frequency domain, or some other cause.

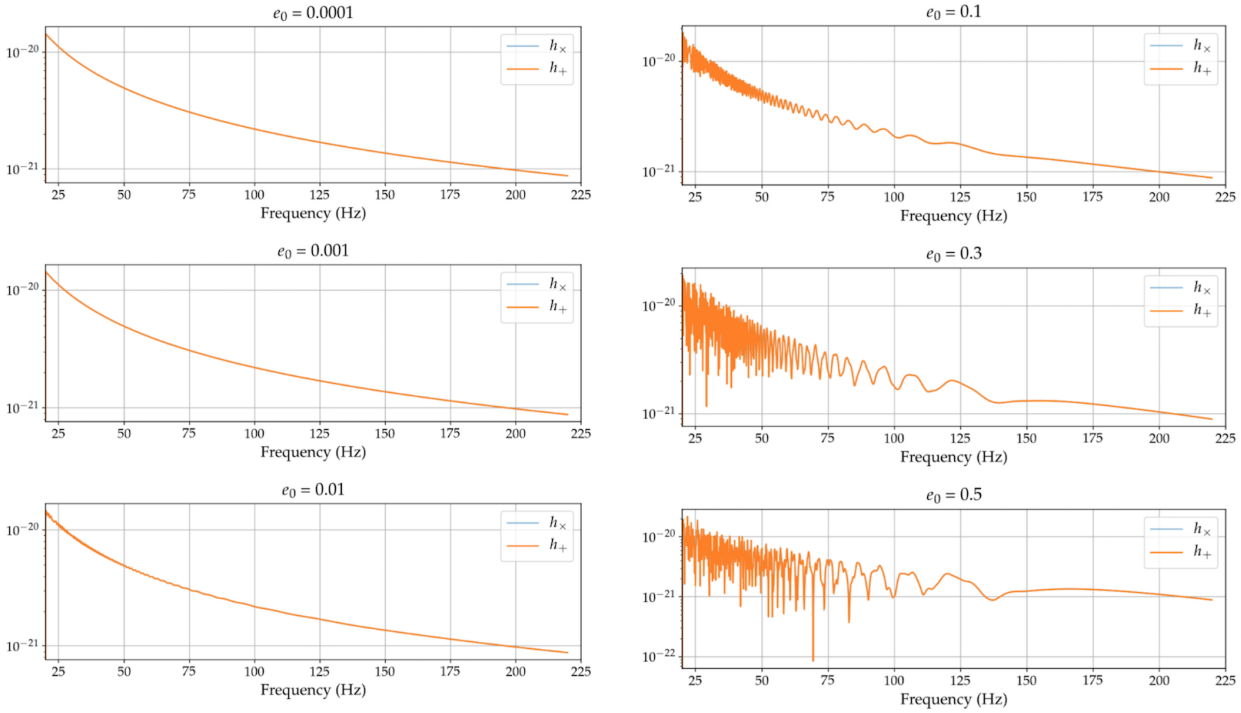

FIG. 10: Magnitude of frequency series waveforms generated with the EccentricFD approximant at initial eccentricities e_0=[0.0001, 0.001, 0.01, 0.1, 0.3, 0.5]. All waveforms are from a source with a distance of 1 megaparsec and masses $m_1 = m_2 = 10M_\odot$. The frequency axis shows the range 20 Hz to 225 Hz. Waveform model from [9].

Models including the merger and ringdown phases of an eccentric CBC *have* been calculated, such as in the paper "Observing complete gravitational wave signals from dynamical capture binaries" by East et al [10]; these models have not yet been incorporated into LALSuite. See Figure 11 for a plot of an example of a full inspiral-merger-ringdown time series.

C. Model Comparison

The waveform model described in Section A (see Figure 8) captures the qualitative features of an eccentric binary inspiral, but is not quantitatively accurate due to several approximations made in the derivation. Such approximations include using Newtonian definitions for energy and angular momentum. The EccentricTD model in LALSuite [9] is likely a more quantitatively accurate waveform template (see Figure 9). Due to being more well tested and de-bugged, we employ the EccentricTD/EccentricFD model for the remainder of this report. However, it is important to note that EccentricTD and EccentricFD do not include spin effects and the EccentricFD waveform looks noisy at high eccentricities for unknown

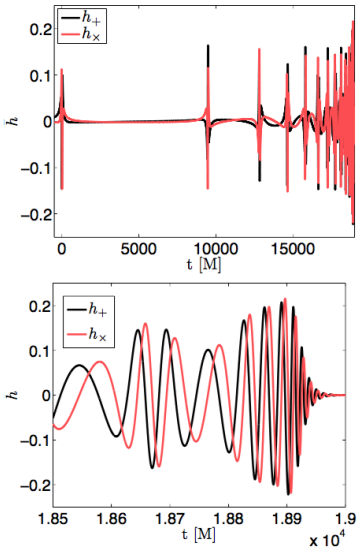

FIG. 11: Gravitational wave strain time series presented by East *et al.* [10] for a periastron $r_p = 0.8M$ and an eccentricity e = 1. The top panel shows the entire waveform; the bottom panel shows a zoomed-in view of the end of the waveform. Note that the time axis is in GR units of M (total mass).

but probably unphysical reasons. To compare my model with EccentricTD, I calculated overlaps between them. The equation to calculate overlap between two vectors a and b is given in (20):

$$\mathcal{O} = \left[\frac{\langle\, a \,|\, b \,\rangle}{\langle\, a \,|\, a \,\rangle^{1/2} \langle\, b \,|\, b \,\rangle^{1/2}} \right]_{max.t,\varphi} \tag{17}$$

where $\langle\, a \,|\, b \,\rangle$ is the noise weighted inner product between a and b, as follows:

$$\langle\, a \,|\, b \,\rangle = 4\Re \int_0^\infty \frac{\tilde{a}(f)\, \tilde{b}^*(f)}{S_n(f)} df \tag{18}$$

where $S_n(f)$ is a power-spectral density (PSD) for the noise in the detector.

In this case, the two vectors a and b are the time series for the strain for my waveform and an EccentricTD waveform with the exact same input parameters. Overlap is a value between 0 and 1, where 1 indicates that a and b are the same vector and 0 indicates that they orthogonal, i.e. completely different vectors. Essentially, the overlap between waveforms is their dot product in the parameter space. Figures 12 and 13 show, in the mass vs. initial eccentricity space, the results of calculating overlap between a waveform generated as described in Section V A and waveform generated using the EccentricTD approximant with the same input parameters. Figure 12 shows overlap over an eccentricity range of 0.05

to 0.45, while Figure 13 zooms in on the low-eccentricity range (0.005 to 0.1), as it is more probable in nature [12]. Note that these overlaps were not maximized over time and phase; if this was done they would likely be higher values.

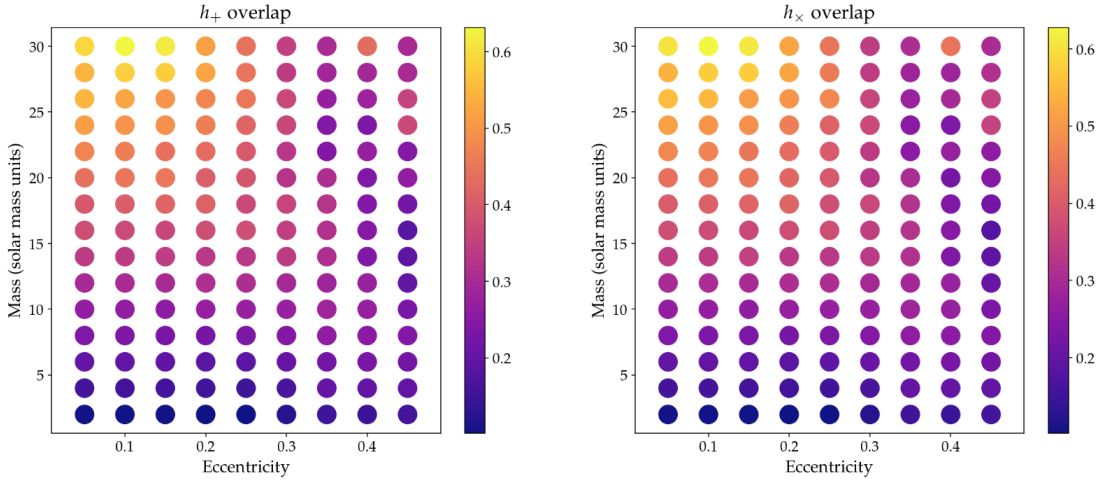

FIG. 12: Overlaps between a waveform generated as described in Section V A and waveform generated using the EccentricTD approximant with the same input parameters. Shown in the input parameter space of mass and eccentricity, with a mass range from 2 - 30 $M_\odot$ sampled every 2 $M_\odot$, and an eccentricity range of 0.05 - 0.45 sampled in increments of an eccentricity of 0.05. Overlaps calculating using *filter* package from [18].

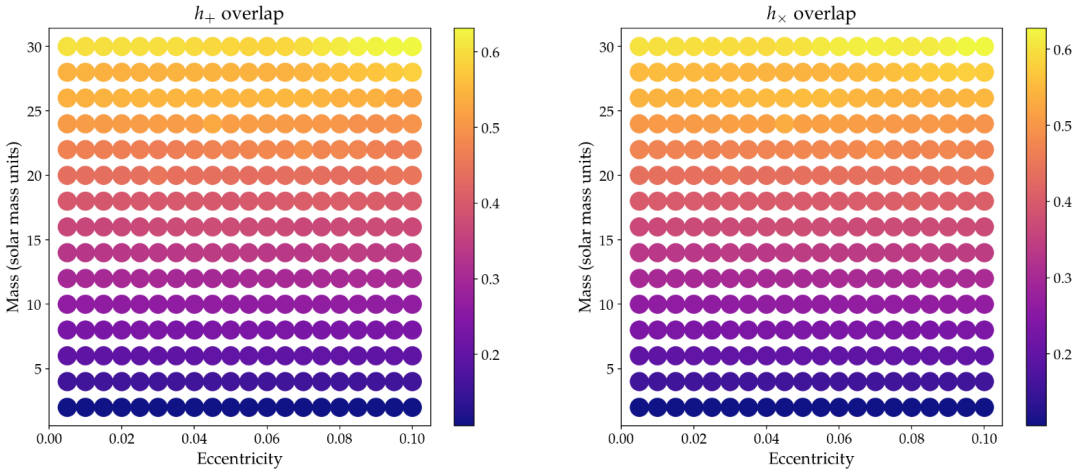

FIG. 13: Same as Fig. 12 but in different eccentricity range and higher sampling rate: a mass range from 2 - 30 $M_\odot$ sampled every 2 $M_\odot$, and an eccentricity range of 0.005 to 0.1, sampled in increments of an eccentricity of 0.005.

The dominant trends in these results are that: as mass increases, the overlap between the two waveforms increases; as eccentricity increases, the overlap decreases. As mass increases, the time the BBH spends in the LIGO band decreases, meaning the time series has less

data points and thus less room for dissimilar data points between the two waveform models. As eccentricity increases, the bursts at periastron passage in the waveform become more pronounced, amplifying any differences between the two waveform models. This behavior is almost identical for both the plus and cross polarizations. The average overlap between the waveforms in the mass range 2 - 30 $M_{\odot}$ is listed in the following table:

e_0 **range**	**No. of samples**	**Average** h_+ **overlap**	**Average** $h_\times$ **overlap**
0.05 to 0.5	150	0.315	0.316
0.005 to 0.1	300	0.366	0.367

VI. PHASE ANGLE EVOLUTION

Since LIGO's matched filtering techniques key in on phase differences between waveforms, understanding the phase evolution of a waveform containing the effects of orbital eccentricity is essential. Additionally, phase can be extracted directly from strain data without first fitting a parameterized template to it. Therefore, phase can be measured without relying on templates of varying credibility. The phase angle φ is extracted from a waveform in the format:

$$h_+ + i\, h_\times = A e^{i\varphi}\,, \tag{19}$$

where h_+ and $h_\times$ are the plus and cross polarizations of the waveform respectively. This φ is the same as the φ as in qquation (6), but *not* the ϕ as in equations (7) and (8). In Figure 14, the phase evolution of waveforms with varying initial eccentricities are plotted.

Subtracting the phase time series of an eccentric waveform from the phase time series of a waveform with negligible eccentricity yields the results seen in Figure 15. The larger the difference in eccentricity between two waveforms, the larger the difference in phase is between them. Additionally, as e_0 increases, the phase difference has a more pronounced sinusoidal component.

Another characteristic of phase that draws interest is its derivative, $\dot{\varphi}$ (see Figure 14 for a plot of the time evolution of $\dot{\varphi}$). The relationship between phase of a gravitational wave and its frequency is:

$$\varphi(t) = \int_0^t 2\,\pi\, f_{GW}(t)\, dt \quad . \tag{20}$$

Therefore, the derivative of the phase is directly proportional to the frequency, $\dot{\varphi}(t) = 2\,\pi\, f_{GW}(t)$. In a non-eccentric case, the frequency of gravitational waves is calculated with equation (21), which is simplified to (22) [17]:

$$f_{GW}(t) = \frac{1}{\pi}\left(\frac{5}{256}\,\frac{1}{t_c\,-\,t}\right)^{3/8}\left(\frac{G\,M_c}{c^3}\right)^{-5/8} \quad , \tag{21}$$

$$f_{GW}(t) = 134\,Hz\left(\frac{1.21\,M_\odot}{M_c}\right)^{5/8}\left(\frac{1}{t_c\,-\,t}\right)^{3/8} \quad . \tag{22}$$

Here, t_c is time of coalescence and M_c is chirp mass: $M_c = \frac{(m_1\ m_2)^{3/5}}{(m_1+m_2)^{1/5}} = \mu^{3/5}\,M_{tot}^{2/5}$. Therefore, the derivative of the phase of a waveform with negligible eccentricity is equivalent to:

$$\dot{\varphi}(t) = 2\,\pi\,134\,Hz\left(\frac{1.21\,M_\odot}{M_c}\right)^{5/8}\left(\frac{1}{t_c\,-\,t}\right)^{3/8} \quad . \tag{23}$$

When using the *curve_fit* function in the Python SciPy package to fit equation (23) to the $e_0 = 0$ $\dot{\varphi}$ curve in Figure 13, we estimated the chirp mass of the system within 3.2% error. This indicates that equation (23) does accurately describe the time-evolution of $\dot{\varphi}$ of a a non-eccentric BBH system. Future work includes deriving an expression for the sinusoidal component of $\dot{\varphi}$ caused by orbital eccentricity. We estimate that the final equation for $\dot{\varphi}$ will be in the following format:

$$\dot{\varphi}(t) = 2\,\pi\, f_{GW}(t) \,+\, \sum_{n=2} g(n, e(t))\, sin(f_{GW}(t)\, t) \tag{24}$$

where $f_{GW}(t)$ is the expression shown in equation (20), and $g(n, e)$ is an expression related to the power distributed in the nth harmonic of a system with eccentricity e.

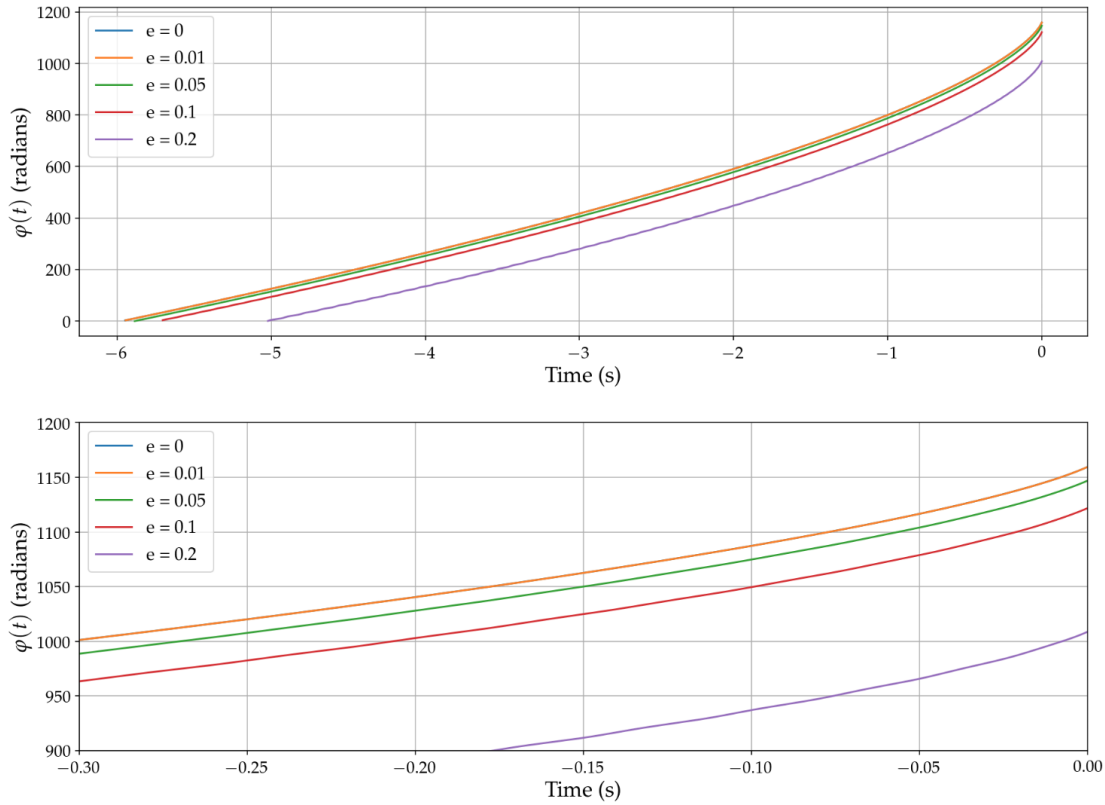

FIG. 14: The phase evolution of EccentricTD waveforms with various eccentricities. All have masses of $m_1 = m_2 = 10M_\odot$, a lower frequency of 20 Hz, and the rest of the parameters set to default. The top panel shows the phase evolution of the entire waveform; the bottom panel zooms in on the last 0.3 seconds before ISCO. In the legend, e refers to the eccentricity when the frequency of emitted GW is 20 Hz.

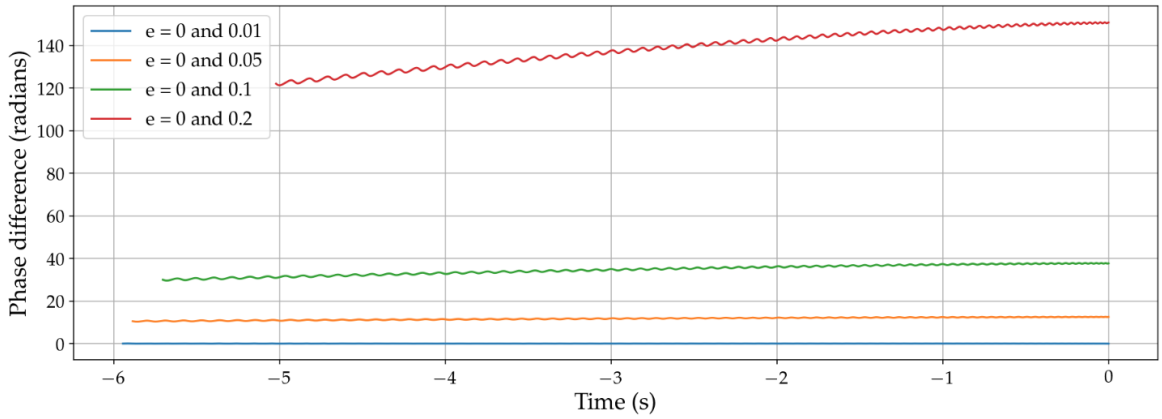

FIG. 15: Time series of the difference in phase between EccentricTD waveforms with and without eccentricity. All waveforms used have masses of $m_1 = m_2 = 10M_\odot$ and a lower frequency of 20 Hz. In the legend, e refers to the eccentricity when the frequency of emitted GW is 20 Hz.

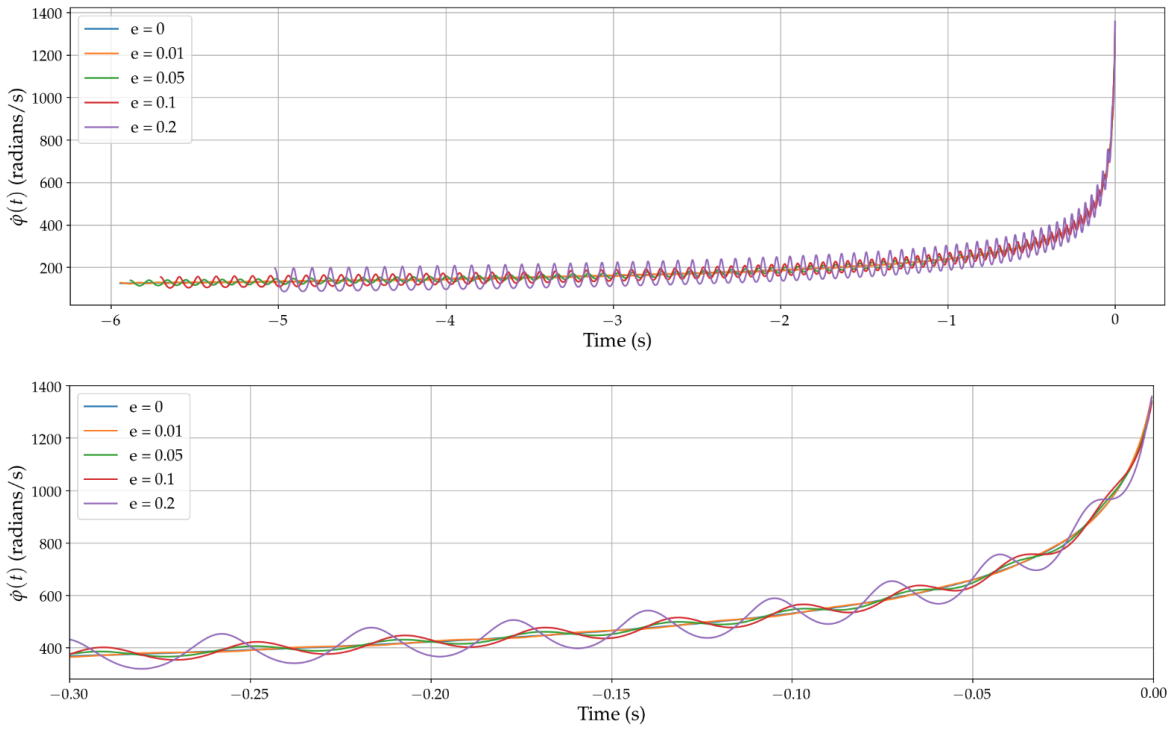

FIG. 16: The derivative of phase evolution for EccentricTD waveforms with various eccentricities. All have masses of $m_1 = m_2 = 10M_\odot$ and a lower frequency of 20 Hz. The top panel shows the derivative of phase evolution of the entire waveform; the bottom panel zooms in on the last 0.3 seconds before ISCO. In the legend, e refers to the eccentricity when the frequency of emitted GW is 20 Hz.

VII. PARAMETER ESTIMATION BAYESIAN FRAMEWORK

Bayesian inference is the leading tool in parameter estimation in gravitational wave science. In the context of GW parameter estimation, data is compared with a parametrized model. Bayes' Theorem can be used to calculate a posterior probability distribution for the model parameters as follows:

$$p(\vec{\theta}\,|\,d, H) = \frac{p(d\,|\,\vec{\theta}, H)\,p(\vec{\theta}\,|\,H)}{p(d\,|\,H)} \tag{25}$$

where $\vec{\theta}$ is a vector containing unknown parameters, $d = \{d_1, d_2, \ldots, d_{\mathrm{N}_f}\}$ are the data represented as strain measurements in N_f discrete frequency bins, and H is a given model. $p(\vec{\theta}\,|\,d, H)$ is the *posterior*, or the probability that the gravitational wave strain was generated by a system with certain set of parameters $\vec{\theta}$ given the data d and assuming a particular model H. $p(d\,|\,\vec{\theta}, H)$ is known as the *likelihood*, also represented with the letter $\mathcal{L}$. The like-

lihood is the probability of measuring the data d given a set of parameters and assuming a particular model. $p(\vec{\theta}\,|\,H)$ is the *prior*, representing prior understanding of the distribution of the parameters in nature. For example, a trivial prior is that an angle must lie between 0 and 2π; a non-trivial prior could be a non-informative or Jeffrey's prior on eccentricity, which is proportional to the square root of the determinant of the Fisher information matrix. Finally, $p(d\,|\,H)$ is the *evidence*, a normalization constant that does not enter into parameter estimation, but that can be used to compare different models using Bayesian Model Comparison [15].

We will assume that the likelihood takes the form of a Gaussian distribution, given as follows for data d and parameters $\vec{\theta}$:

$$\mathcal{L} = p(d\,|\,\vec{\theta}) = \mathcal{N}\exp\left(-\frac{1}{2}\langle h(\vec{\theta}) - d\,|\,h(\vec{\theta}) - d\rangle\right) \tag{26}$$

where $h(\vec{\theta})$ is the gravitational wave strain generated by a system with parameters $\vec{\theta}$ and $\mathcal{N}$ is an arbitrary constant that gets canceled out by the evidence term in the posterior distribution [16]. The noise weighted inner product $\langle\, a\,|\,b\,\rangle$ is given in equation (18). Note that the the data d is a sum of the signal + Gaussian noise, meaning $h(\vec{\theta}) - d$ represents the Gaussian distribution of the noise. Additionally, the likelihood is maximized over time and phase of coalescence.

VIII. USING A QUASI-CIRCULAR WAVEFORM TEMPLATE TO EXTRACT AN ECCENTRIC SIGNAL

Currently, due to the absence of full inspiral-merger-ringdown waveform templates in LALSuite that include the effects of eccentricity, if an incoming GW signal *was* created by BBH system with non-negligible eccentricity, LIGO's data analysis methods would be performed assuming that the system was quasi-circular. That is, the templates used in both the search and parameter estimation pipelines include inspiral-merger-ringdown and spin, but an initial eccentricity equal to 0. Ignoring eccentricity results in a signal with a lower signal to noise ratio (SNR) and compromises our ability to accurately estimate the other parameters of the system, introducing biases in data.

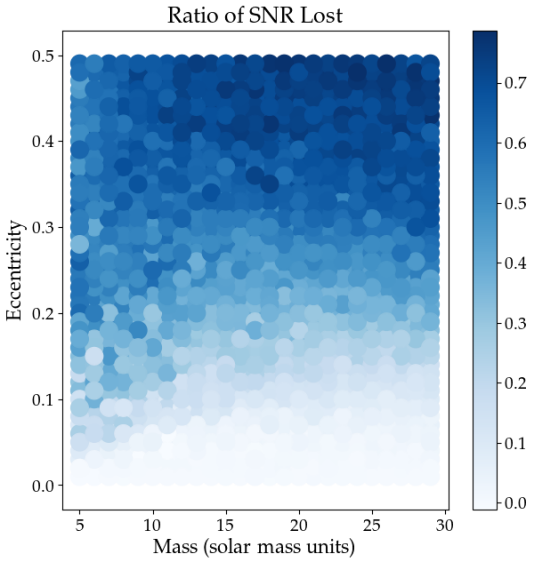

FIG. 17: Ratio of SNR lost ($\text{SNR}_{ecc}-\text{SNR}_{circ}/\text{SNR}_{ecc}$) when using a template with no eccentricity to recover a waveform with eccentricity and the same mass parameters as the non-eccentric template. Shown in the input parameter space of mass vs. initial eccentricity of the injection, with a mass range from 5 - 30 $M_\odot$ sampled every 1 $M_\odot$, and an eccentricity range of 0.01 to 0.5, sampled in increments of an eccentricity of 0.01.

A. Lost SNR

The higher the eccentricity, the more SNR is lost when trying to recover this waveform using a quasi-circular template. At initial eccentricities of 0.3 and higher, around 60% of the SNR could be lost. At an initial eccentricity of 0.5, 80% or higher of the SNR could be lost. This is shown in Figure 17. This means we could be missing a class of low-SNR signals entirely just by assuming they are circular.

B. Parameter Estimation for Mass

In addition to causing a loss in SNR, extracting an eccentric signal with a circular waveform template yields inaccurate estimations for other parameters. In this project, we focused on this effect on the total mass of the system. As can be seen in Figure 18, as the initial eccentricity of the injected signal (e_0) increases, the likelihood curve, computed with noiseless data and maximized over time and phase of coalescence, for total mass peaks at values further and further from the actual injected mass. For example, at an injected e_0 of 0.1, the

circular likelihood curve peaks up at a total mass 0.04 solar masses higher than the injected total mass. At this injected e_0, the actual injected mass of 10 $M_\odot$ is not even in the 90% confidence interval of the distribution.

This bias in the parameter estimation is small, but non-negligible, especially considering the sharpness of the peaks of the likelihood curves. The cause of this degeneracy is the fact that, despite causing very different modulations of waveform amplitude and frequency, the dominant effect of both increasing total mass and increasing initial eccentricity is decreasing the duration of the waveform in the LIGO band.

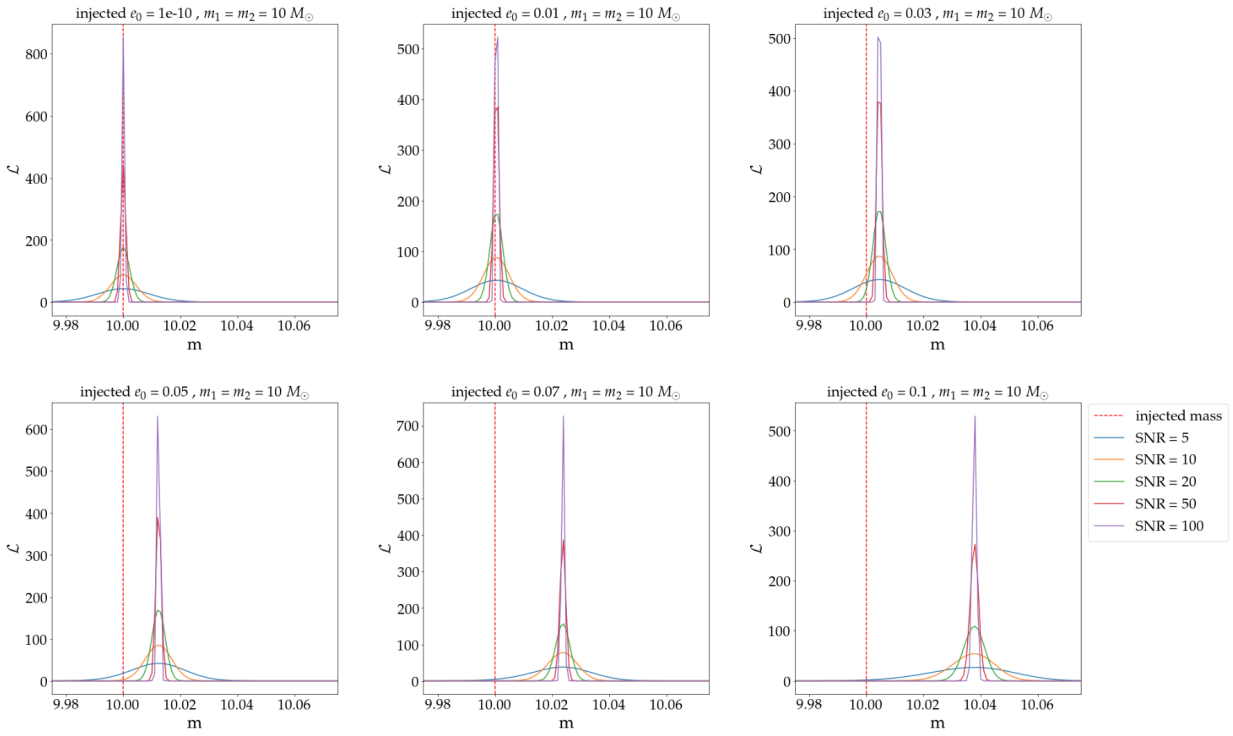

FIG. 18: One-dimensional likelihood distribution for total mass (with $m_1 = m_2$), made by recovering an EccentricTD injection at various e_0 values with an EccentricTD waveform with $e_0 = 0$ and all other parameters the same. Likelihood curve calculated with equation (26) using *pycbc.inference* Python package.

IX. USING AN ECCENTRIC WAVEFORM TEMPLATE TO EXTRACT AN ECCENTRIC SIGNAL

In this section, we seek to discover how well the eccentricity parameter could extracted from an observed event when using a eccentric template to recover the waveform. As men-

tioned in Section VIII, these calculations only account for the inspiral phase of the waveforms, for at the current moment since there are no full inspiral-merger-ringdown waveforms implemented in LALSuite. We use EccentricTD for both injections (with added Gaussian noise from the aLIGO design noise curve) and models.

A. One Dimensional Parameter Estimation

Here, we calculate a likelihood distribution using equation (26) in just the one-dimensional parameter space of eccentricity, assuming all other parameters are known. Results from these calculations are shown in Figure 19, at a range of different injected e_0, M_{tot}, and SNR. Our results indicate that as total mass decreases and/or SNR increases, the one dimensional likelihood curves for eccentricity peak more sharply, indicating that e_0 can be estimated more accurately. When $e_0 = 10^{-3}$, e_0 is indistinguishable from 0 regardless of SNR, indicating that we cannot measure eccentricities on this order of magnitude. However, if a signal has a large SNR (i.e. greater than about 20), then our results indicate that we *can* measure eccentricities on the order $e_0 = 10^{-2}$. By the time $e_0 = 10^{-1}$, the peaks are very sharp; at SNR > 5, eccentricities on this order of magnitude are completely distinguished from eccentricities of 0. In the following section, IX B, we further explore what combinations of SNR and eccentricity are inconsistent with an eccentricity of 0.

B. When is a non-zero eccentricity distinguishable from $e_0 = 0$?

Confidence intervals are a means means of measuring which range of parameter values encompass a certain percentage of the posterior distribution. Here, we use a likelihood distribution instead of a posterior distribution because we assume a Jeffrey's prior (flat prior) for eccentricity, so the posterior distribution and likelihood distribution are identical. For example, the 90% confidence interval for estimating a the value of a particular parameter is the area under 90% of the likelihood curve, starting at the peak and going outwards symmetrically in e_0 - i.e. we can be 90% sure that the value we are measuring for a parameter falls within that range. If the likelihood curve is normalized, the area under the 90% confidence interval of the curve equals 0.9.

Here, we use confidence intervals to classify at what confidence level we can say a measured

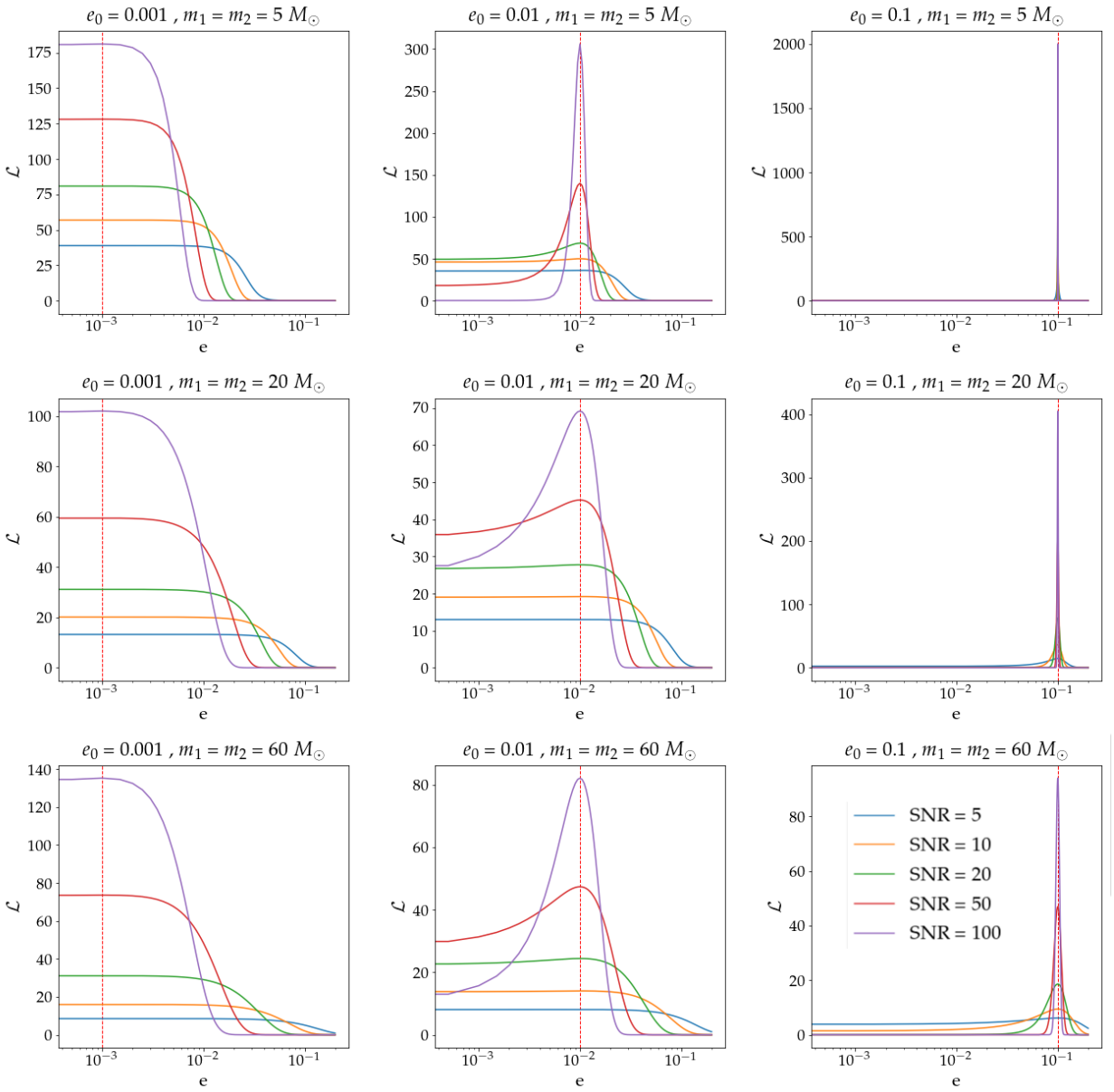

FIG. 19: One-dimensional likelihood distributions for recovering an EccentricTD injection with $e_0 = \{0.001, 0.01, 0.1\}$, $m_1 = m_2 = \{5, 20, 60\} M_\odot$, and SNR = {5, 10, 20, 50, 100} using an EccentricTD waveform with all parameter values fixed except eccentricity. The eccentricity axis is on a log scale. Likelihood curve calculated using equation (26).

eccentricity is non-zero at a given SNR. Integrating across windows centered on the likelihood peak, we calculated the area under the likelihood curve until reaching $e = 0$. If $e = 0$ is very close to the peak of the curve, the confidence level will be low (for example, 20% or 0.2); alternately, if $e = 0$ is very far from the peak, it essentially doesn't fall under the likelihood curve at all, leading to a confidence level of 99+% or 0.9999... .

Results from these calculations at injected SNRs ranging from 5 to 100 and initial eccentricities from 0.0 to 0.1 can be seen in Figures 20 and 21. We conclude that at a reasonable SNR, of say 10, initial eccentricities of down to 0.05 are inconsistent with zero at $\sim 90\%$ confidence, assuming all other parameters are known. At every SNR plotted here, eccentricities of 0.1 are inconsistent with zero at 90+% confidence. These results show that incorporating the eccentricity parameter in LIGO's waveform templates in LALSuite is essential, as it is an effect that is detectable down at an order of magnitude of 10^{-2} or least 10^{-1}.

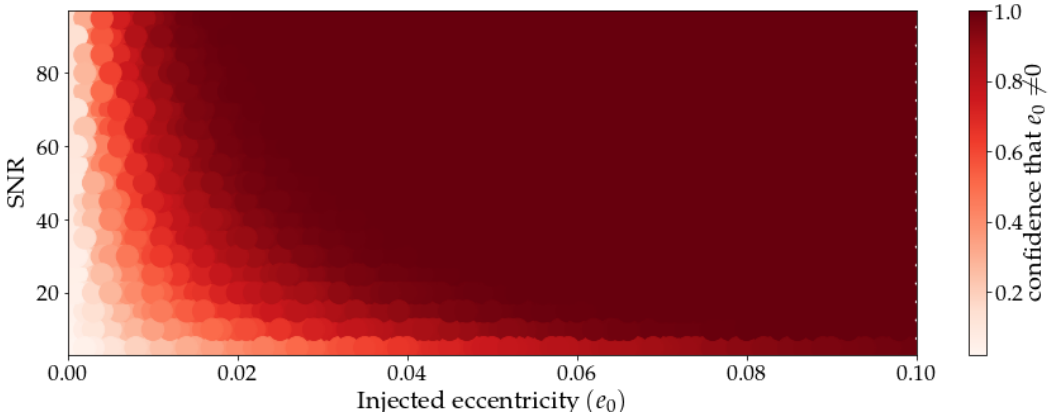

FIG. 20: Confidence that $e_0 \neq 0$ as a function of e_0 and SNR. All waveforms generated using EccentricTD with $M_{tot} = 20M_{\odot}$, $f_{low} = 20$ Hz, and with Gaussian noise from the Advanced LIGO Design noise curve. SNR plotted from 5 to 100, sampled in intervals of 0.5; e_0 plotted from 0 to 0.1, sampled in intervals of 0.001.

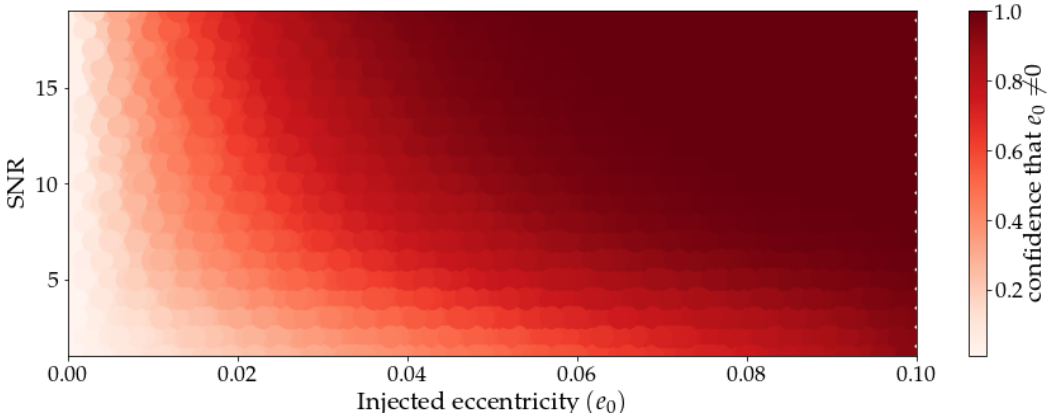

FIG. 21: Same plot as Figure 20, but zoomed in on lower SNR signals (SNR < 20). SNR plotted from 0 to 20, sampled in intervals of 1; e_0 plotted from 0 to 0.1, sampled in intervals of 0.0005.

C. Two Dimensional Parameter Estimation

Realistically, parameter estimation is never done in just one dimension. Full gravitational wave parameter estimation has a minimum of fifteen parameters, not even including eccentricity or other higher order effects. Here, we look in a two-dimensional parameter space of eccentricity and some mass parameter (either total mass or mass ratio), at various combinations of SNR, injected mass, and injected initial eccentricity.

1. *Total Mass (M_{tot})*

Results from two-dimensional parameter estimation for total mass and eccentricity can be seen in Figures 22-24. Figure 22 shows three plots of likelihood surfaces for signals with same the SNR and total mass but different injected initial eccentricities. As eccentricity increases, the likelihood curve becomes much sharper, but with a stronger degeneracy with mass. Figure 23 shows data from four signals with the same SNR and injected e_0 but different total masses. As total mass increases the likelihood peak becomes less sharp. This means we can estimate both eccentricity and mass more accurately in lower mass systems. Finally, Figure 24 shows data from signals with the same injected eccentricity *and* mass but at different SNR. As expected, as SNR increases the likelihood curve retains the same shape but is sharper (spans less of the parameter space).

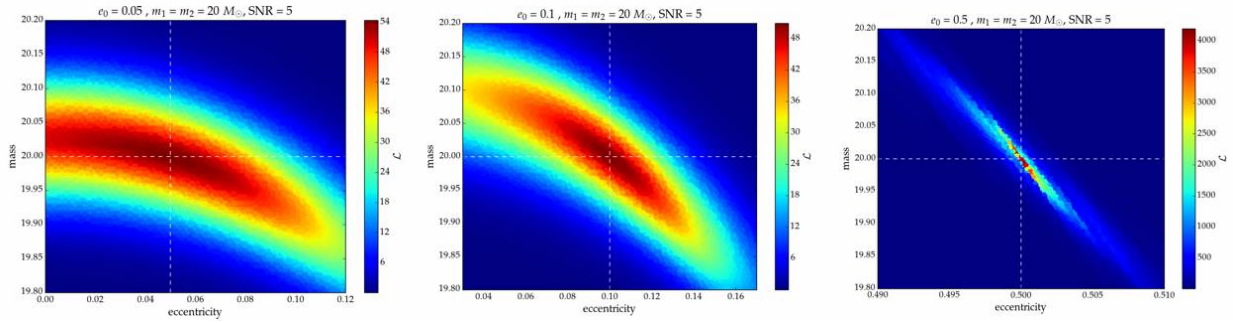

FIG. 22: 2-dimensional likelihood distributions in the total-mass-and-eccentricity parameter space for fitting an EccenticTD waveform to an injection generated with EccentricTD with Gaussian noise from the aLIGO Design noise curve with SNR = 5, $m_1 = m_2 = 20M_\odot$, and $e_0 = \{0.05, 0.1, 0.5\}$. The dashed white lines represent injected parameter values.

All of our data here displays the expected degeneracy between total mass and eccentricity. If no degeneracy was present, the data would look like 'circular' spread around the

injected value; instead, it is a diagonal 'elliptical' spread. As mentioned in Section VIII, this degeneracy is caused by the fact that the dominant effect of both increasing total mass and increasing initial eccentricity is decreasing the duration of the waveform in the LIGO band. This means that systems with a slightly lower eccentricity and larger mass or slightly higher eccentricity and smaller mass produce waveforms of similar duration.

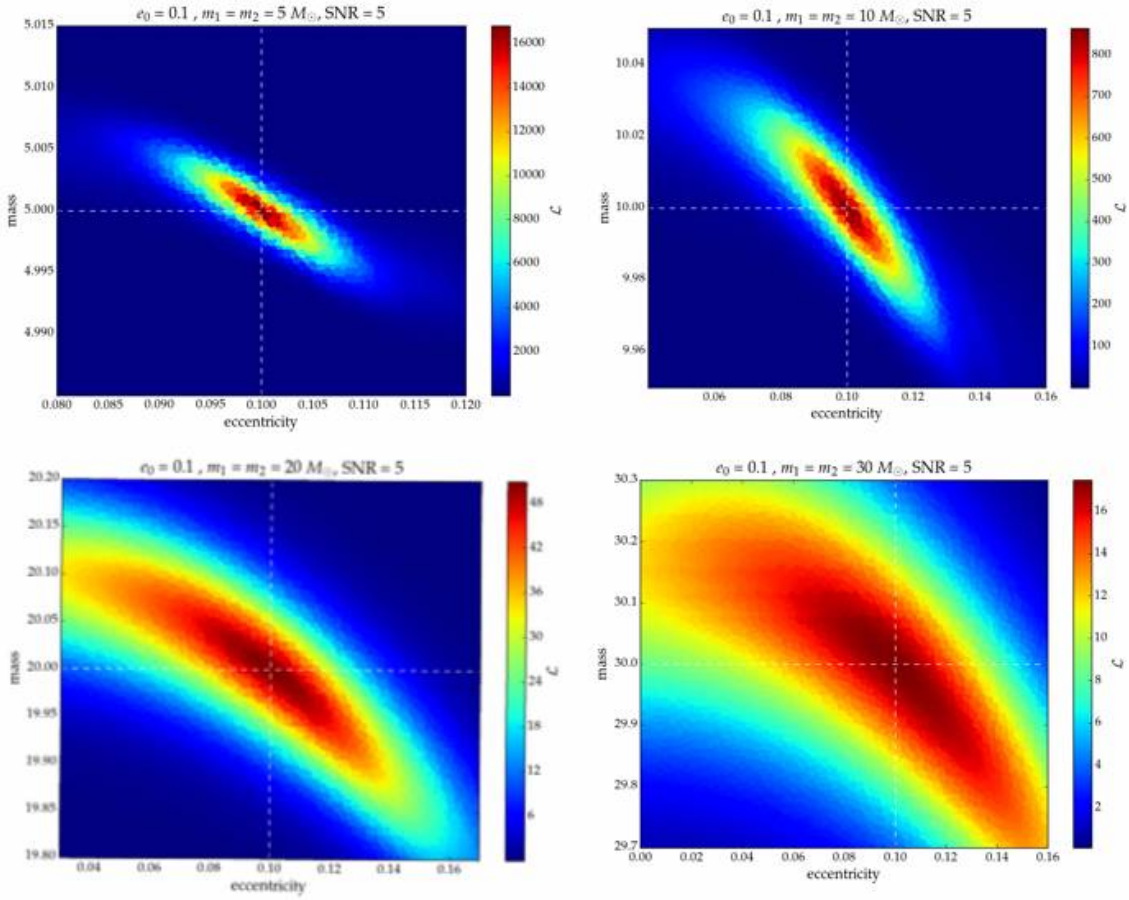

FIG. 23: Same as Fig 22. but with SNR = 5, $e_0 = 0.1$, and $m_1 = m_2 = \{5, 10, 20, 30\}M_\odot$.

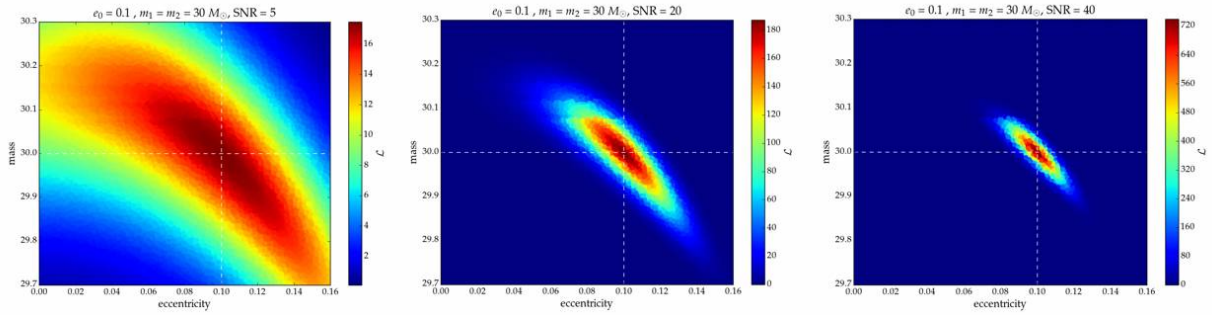

FIG. 24: Same as Fig. 22 and 23 but with $m_1 = m_2 = 20M_\odot$, $e_0 = 0.1$, and SNR = $\{5, 20, 40\}$.

When incorporating more than one parameter into Bayesian parameter estimation, the one dimensional likelihood curve for every parameter is wider than it would be if all other parameters were somehow known. This is shown in Figure 25, where we compare an example of a one dimensional likelihood curve for eccentricity for the same signal where we "know" the total mass of the system versus when we calculate a two dimensional likelihood curve in the mass-eccentricity parameter space and then project the curve onto the eccentricity axis and re-normalized. This is called "marginalizing over mass."

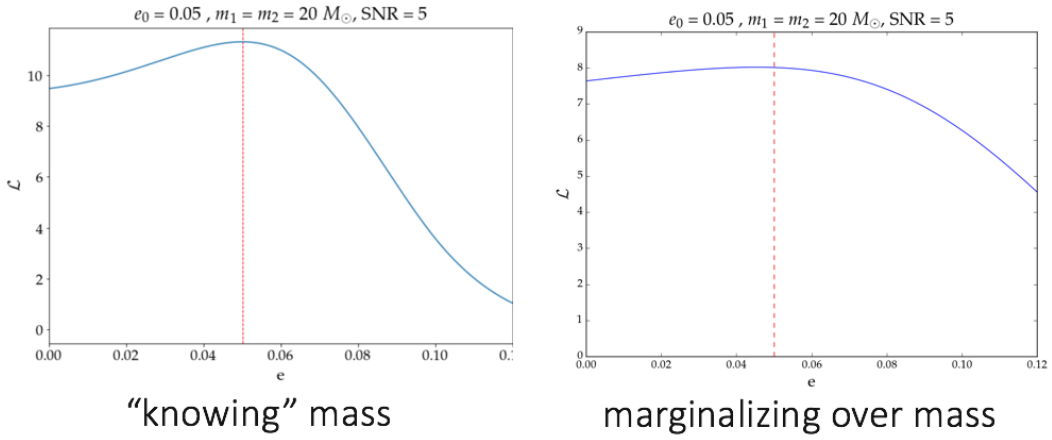

FIG. 25: One dimensional likelihood plots for eccentricity in a system with an initial eccentricity of 0.05, a total mass of 40 $M_\odot$, a mass ratio of 1, and an SNR of 5. The top plot is made with eccentricity as the only free variable; the bottom plot has both eccentricity and mass as free variables and is marginalized over mass.

2. Mass Ratio (q)

In addition to exploring the two dimensional parameter space of total mass and eccentricity with a fixed mass ratio q of 1, we looked at the mass-ratio-and-eccentricity parameter space at a fixed total mass value. Here, $q \equiv m_2/m_1 \leq 1$. Therefore a mass ratio of, say, 0.5 means that m_1 is twice as large as m_2. Just like a larger total mass, a larger mass ratio also decreases the duration of a gravitational waveform in the LIGO band. This bias can be seen in Figure 26. The left and middle plots in Figure 26 have the same total mass but different mass ratios, while the middle and right plots have the same mass ratio but different total masses. At smaller mass ratios, the likelihood curve is narrower in both the mass-ratio and eccentricity dimensions. At larger total masses, there is less of a degeneracy between mass ratio and eccentricity; the likelihood distribution is wider in the mass-ratio dimension.

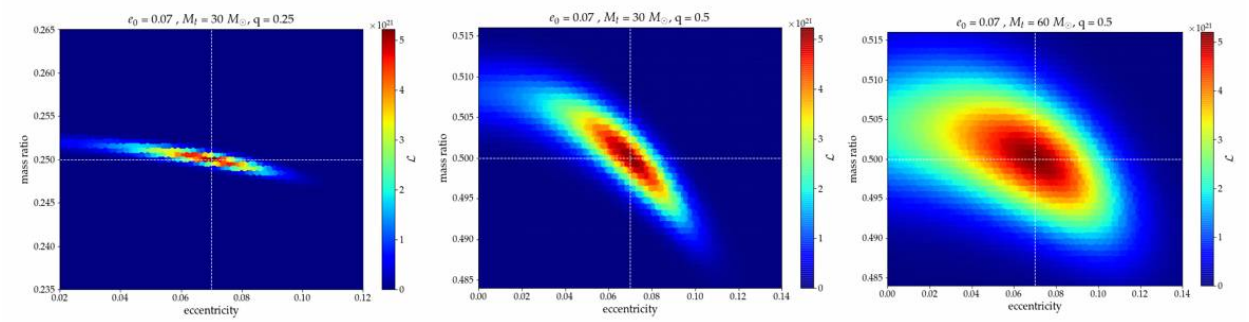

FIG. 26: 2-dimensional likelihood distributions in the mass-ratio-and-eccentricity parameter space for fitting an EccenticTD waveform to an injection generated with EccentricTD with Gaussian noise from the aLIGO Design noise curve with e_0=0.7, SNR=10, and either $M_{tot} = 30M_\odot$, $q = 0.25$ (left); $M_{tot} = 30M_\odot$, $q = 0.5$ (middle); or $M_{tot} = 60M_\odot$, $q = 0.25$ (right). The dashed white lines represent injected parameter values.

X. USING A PRECESSING-SPIN WAVEFORM TEMPLATE TO EXTRACT AN ECCENTRIC SIGNAL

The final portion of this project was beginning the early stages of searching for degeneracies not just between parameters, but between waveform models. There are currently not inspiral-merger-ringdown models in LALSuite that incorporate the effects of eccentricity, but there *are* models including other higher order effects like spin precession. As such, it is possible to study whether eccentricity could be mistaken for another effect. Here we use LALInference, a LAL Bayesian inference pipeline, to perform parameter estimation on an injected eccentric signal (generated with EccentricTD) using a precessing spin waveform, specifically IMRPhenomPv2pseudoFourPN. In order to ensure that the only the inspiral phase of the IMRPhenomPv2pseudoFourPN waveforms were considered in the posterior calculations, we implemented a high frequency cutoff.

Our preliminary results come from two LALinference runs: one where the injected waveform had negligible eccentricity ($e_0 = 10^{-10}$), and one with a non-negligible initial eccentricity of 0.1. The results for the parameter estimation for total mass (M_{tot}), chirp mass (M_c), and two spin parameters $\chi_{effective}$, and χ_p from these runs can be seen in Figures 27 and 28 respectively.

The posterior curves from the injection with negligible eccentricity should peak at the injected values for the parameters, indicated by the blue dashed lines on the corner plots; however, they do not. Thus, we hypothesize that the two waveform models - EccentricTD

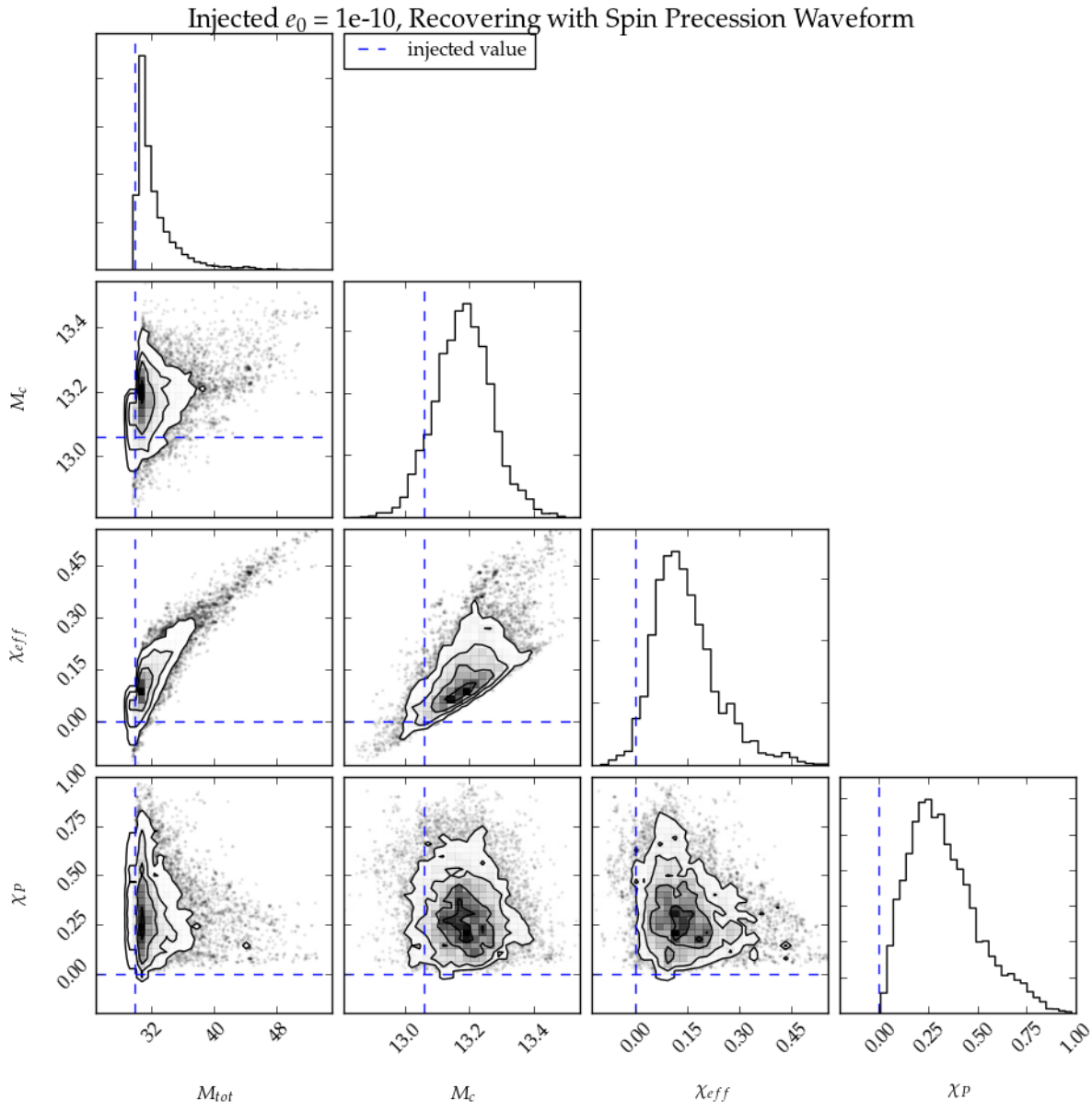

FIG. 27: LALInference results for M_{tot}, M_c, χ_{eff}, and χ_p from EccentricTD injection with negligible eccentricity, recovered with IMRPhenomPv2pseudoFourPN spin-precessing waveform.

and IMRPhenomPv2pseudoFourPN - are different even in the case of negligible eccentricity and negligible spin. We investigated this further and discovered that in the frequency domain, EccentricTD does not align with either IMRPhenomPv2pseudoFourPN or other spinning waveforms regardless of initial eccentricity. One of these comparisons can be seen in Figure 29, between EccentricFD and SEOBNRv2, another approximant that includes spin. EccentricFD seems especially "noisy" whenever the eccentricity is non-negligible. As aforementioned, we are unsure if this effect has physical causes. The overlaps (see equation

17) between the EccentricTD and the various spinning waveforms was always less than 0.1, meaning they are very dissimilar.

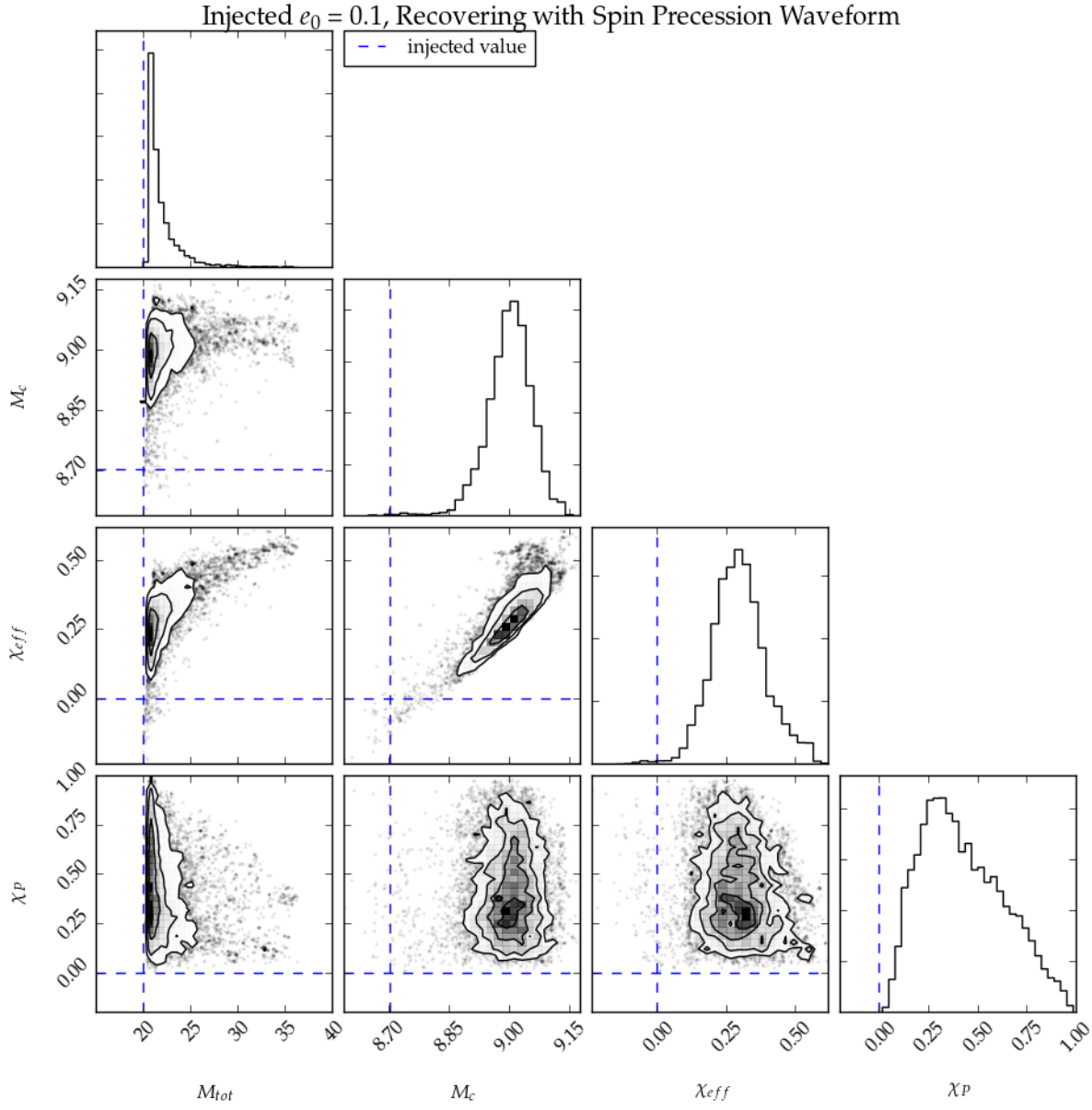

FIG. 28: LALInference results for M_{tot}, M_c, χ_{eff}, and χ_p from EccentricTD injection with initial eccentricity of 0.1, recovered with IMRPhenomPv2pseudoFourPN spin-precessing waveform.

Despite indications that EccentricTD might not be a reliable waveform model, we continue to use it in our analyses because it is the only waveform in LALSuite that incorporates eccentricity. The results from the LALInference run from the injection with an initial eccentricity of 0.1 indicate that a degeneracy could exist between spin precession and eccentricity. The posterior distributions in Figure 28 peak further from the injected values than they do

in plots from the run with non-negligible eccentricity. In case with an eccentric injection, the true parameter values predominantly fall outside of the 90% confidence interval of the posterior distributions. The bias in the mass-parameter posteriors is consistent with our knowledge that larger mass and eccentricity both shorten the duration of the waveform in the LIGO band, as has been previously mentioned. Larger spin-parameter values *also* have this effect, which could explain why the χ_{eff} posterior distribution peaks at a higher value in the plot from the eccentric injection than the non-eccentric injection. Additionally, unlike the likelihood distributions plotted in previous sections, these posterior distributions include the weighted effect of priors on the parameters, which could explain the particular shapes of the distributions. For example, the distribution for M_{tot} in Figure 28 is running up against some lower-limit on the prior for total mass.

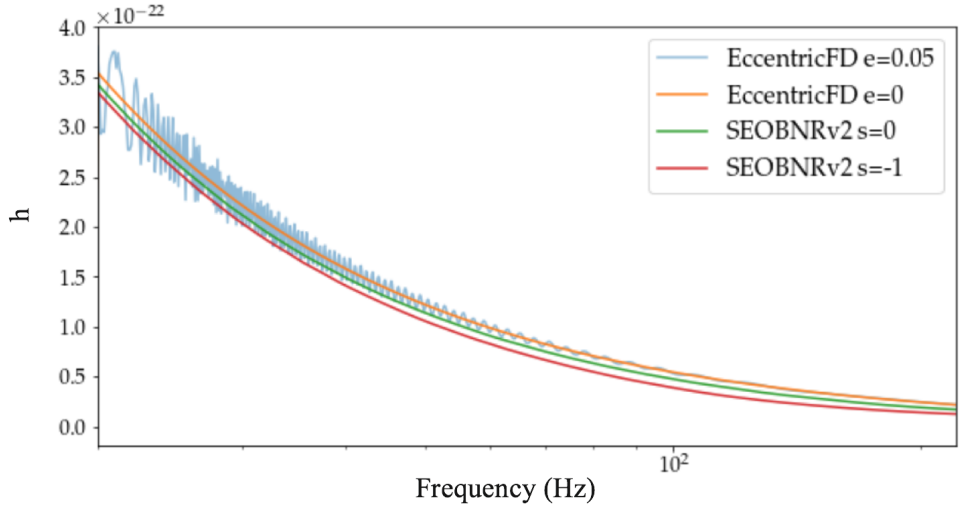

FIG. 29: Strain magnitude $|\tilde{H}(f)|$ for EccentricFD and SEOBNRv2 (a spinning waveform) plotted in the frequency domain (log scale) with various values of eccentricity and spin.

XI. CONCLUSIONS

In this project, we modeled eccentricity in the gravitational waveforms emitted by binary black hole systems and investigated the detectability and measurability of this parameter. Understanding and measuring eccentricity is essential for determining BBH formation mechanisms. Orbital eccentricity modulates both the amplitude and the frequency of a gravitational waveform. Gravitational wave bursts at periastron passage, causing spikes in amplitude in the waveform, are a characteristic effect of orbital eccentricity. Additionally,

eccentric waveforms have a unique sinusoidal component in the time evolution of the derivative of their phase-angle. Continuing to derive a model-independent statistic for this effect is in the future work for this project.

Performing parameter estimation on an eccentric signal using a quasi-circular waveform template causes a loss in SNR compromises our ability to accurately estimate other intrinsic parameters (e.g. mass parameters) of the system. However, our results indicate that at reasonable SNR (e.g. $\sim$10) we can detect eccentricities of down to $\sim$0.04 with $\sim$90% confidence, assuming all other parameters are known. This lower limit is higher when more parameters are marginalized over. Additionally, we determined that orbital eccentricity is somewhat degenerate with both total mass and mass ratio of the BBH, as the dominant effect of increasing all three of these parameters is decreasing the duration of the signal in the LIGO band. Another future direction for this project is continuing using LALInference to search for degeneracies between eccentricity and other higher order effects.

XII. ACKNOWLEDGEMENTS

I would like to acknowledge the Laser Interferometer Gravitational-wave Observatory (LIGO), the LIGO Scientific Collaboration (LSC), LIGO Laboratory at California Institute of Technology, and the Caltech Student-Faculty Programs (SFP) and Summer Undergraduate Research Fellowship (SURF) for the incredible opportunity to conduct this research this summer. I would especially like to thank Alan Weinstein, Jonah Kanner, and Thomas Callister for their mentorship and my fellow LIGO SURF students for their comradery and support.

---

[1] Abbott, B., et al. (LIGO Scientific Collaboration), "Astrophysical Implications of the Binary Black-Hole Merger GW150914," *Astrophys. J.*, LIGO-P1500262, (2016), [arXiv:1602.03846v1].

[2] Abbott, B., et al. (LIGO Scientific Collaboration and Virgo Collaboration), "Binary Black Hole Mergers in the First Advanced LIGO Observing Run," *Phys. Rev. X*, **6**, 041015, (2016).

[3] Abbott, B., et al. (LIGO Scientific Collaboration and Virgo Collaboration), "GW151226: Observation of Gravitational Waves from a 22-Solar-Mass Binary Black Hole Coalescence," Phys. *Rev. Lett.* **116**, 241103, (2016).

[4] Abbott, B., et al. (LIGO Scientific Collaboration and Virgo Collaboration), "GW170104: Observation of a 50-Solar-Mass Binary Black Hole Coalescence at Redshift 0.2" *Phys. Rev. Lett.* **118**, 221101 (2017).

[5] Abbott, B., et al. (LIGO Scientific Collaboration and Virgo Collaboration), "GW170608: Observation of a 19 Solar-mass Binary Black Hole Coalescence", *Astrophys. J.* **35**, 11pp (2017).

[6] Abbott, B., et al. (LIGO Scientific Collaboration and Virgo Collaboration), "GW170814: A Three-Detector Observation of Gravitational Waves from a Binary Black Hole Coalescence" *Phys. Rev. Lett.* **119**, 141101 (2017).

[7] Sathyaprakasch, B.S and Bernard F. Schutz, Physics, Astrophysics, and Cosmology with Gravitational Waves, *Living Rev. Relativity*, lrr-2009-2, (2009): http://www.livingreviews.org/lrr-2009-2.

[8] LIGO Open Science Center, Data release for event GW150914, https://losc.ligo.org/events/GW150914/

[9] LALSuite: Main Page, https://lscsoft.docs.ligo.org/lalsuite/

[10] East, William B., et al. "Observing complete gravitational wave signals from dynamical capture binaries", *Phys. Rev. D*, 87 (2013), [arXiv:1212.0837v2]

[11] Randall, Lisa and Zhong-Zhi Xianyu. "Induced Ellipticity for Inspiraling Binary Systems,"An Analytical Portrait of Binary Mergers inHierarchical Triple Systems," (2018) [arXiv:1802.05718v1]

[12] Lower, Marcus E., et al. "Measuring eccentricity in binary black hole inspirals with gravitational waves," (2018)

[13] Blanchet, Luc. "Gravitational Radiation from Post-Newtonian Sources and Inspiralling Compact Binaries," *Living Rev. Relativity*, **17** /lrr-2014-2 (2014):http://www.livingreviews.org/lrr-20014-2.

[14] Callister, Thomas A. "Improving Models of Eccentric Compact Binary Inspirals," University of Cambridge, (2014).

[15] Biwer, C. M., et al. "PyCBC Inference: A Python-based parameter estimation toolkit for compact-object merger signals," (2018).

[16] Thrane, Eric and Colm Talbot. "An introduction to Bayesian inference in gravitational-wave astronomy: parameter estimation, model selection, and hierarchical models," (2018) [arXiv:1809.02293v2]

[17] Maggiore, Michele. *Gravitational Waves: Theory and Experiments*, Volume 1, Oxford University Press, (2008).

[18] PyCBC: Free and open software to study gravitational waves, https://pycbc.org/

[19] Randall, Lisa and Zhong-Zhi Xianyu. "Induced Ellipticity for Inspiraling Binary Systems," (2018), [arXiv:1708.08569v2]

[20] Samsing, Johan. "Eccentric Black Hole Mergers Forming in Stellar Clusters," (2017), [arXiv:1711.07452]

[21] Tiwari, V., et al. "A Proposed Search for the Detection of Gravitational Waves from Eccentric Binary Black Holes," *Phys. Rev. D*, 93 (2016), [arXiv:1511.09240]

[22] scipy.optimize.curve_fit. *SciPy.org*.https://docs.scipy.org/doc/scipy/reference/generated/scipy.optimize.curve_fit.html

[23] LALInference: Main Page, https://lscsoft.docs.ligo.org/lalsuite/lalinference/index.html